



Changes in the South American Monsoon System components since the Last Glacial Maximum: a TraCE-21k perspective

Igor Stivanelli Custódio¹ · Pedro Leite da Silva Dias¹ · Ilana Wainer² · Luciana F. Prado³

Received: 26 September 2022 / Accepted: 29 January 2024 / Published online: 5 March 2024
© The Author(s), under exclusive licence to Springer-Verlag GmbH Germany, part of Springer Nature 2024

Abstract

The main objective of this study is to investigate the spatial–temporal variability and climate forcing influence during the last 21,000 years of the South American Monsoon System (SAMS) and its components. TraCE-21k simulations, including Full and Single Forcings experiments, were employed. The identification of spatial variability patterns associated with the core of the monsoon region (SAMS) and the South Atlantic Convergence Zone (SACZ), the main components of SAMS during the austral summer, is based on multivariate EOF analysis (precipitation, humidity, zonal and meridional wind). This analysis produces two main modes: the first one is the South American Large Scale Monsoon Index (LISAM), representing the primary oscillation mode for SAMS, and the second one is the SACZ mode, representing the SACZ oceanic portion variability. The TraCE-21k EOF modes demonstrated the ability to represent the SAMS and SACZ patterns when compared to the 20th Century reanalysis. LISAM time series proved to be an important tool for identifying monsoon precipitation variability, consistent with the regime changes recorded in climatic proxies. The freshwater pulses forcing in TraCE-21k are a determining factor for the observed changes in the precipitation regime, mainly during the periods between Heinrich Stadial 1 and the Younger Dryas. The results indicate that the observed and modeled SACZ southward shift in the Late Holocene is primarily modulated by insolation changes, with a stronger correlation observed since the Mid-Holocene period. Through wavelet analysis, it was noted that energy was transferred from low frequencies to high frequencies during the Bølling–Allerød period for the full forcing and freshwater pulse experiments in the Northern Hemisphere. The SAMS multidecadal variability increased from the early Holocene with direct influences of orbital forcing and ice cover.

Keywords Paleoclimate · LISAM · Variability · South America · Single forcings · Monsoon · TraCE-21k simulations

1 Introduction

Climate variability directly or indirectly impacts human activities. There are various types of climate variability, including those associated with natural and anthropogenic sources. The former relates to changes intrinsic to the climate system, while the latter is attributed to changes caused by human activities. South American (SA) paleoclimatic records offer evidence of natural climate variability. Proxies

indicate no significant anthropogenic influence before the Holocene, providing a much-extended period compared to the instrumental record. These records also exhibit reasonable spatial data distribution, presenting an excellent opportunity to evaluate the performance of climate models and offer validation for IPCC-class models (Braconnot et al. 2012).

Most of the tropical region of South America is characterized by a well-defined annual cycle of precipitation, with significant contrasts between the austral summer (rainy during December–January–February/DJF) and winter (dry during June–July–August/JJA), except in Northeast Brazil (NEB) and the extreme North Region of Brazil (NB) which are not influenced by SAMS. Several studies have demonstrated that the most significant component of South America's summer precipitation regimes originates from the South American Monsoon System (SAMS). This system develops in low-latitude continental regions in response to seasonal changes in thermal contrast between the continent

✉ Igor Stivanelli Custódio
iscustodio@alumni.usp.br

¹ Institute of Astronomy, Geophysics and Atmospheric Science, University of São Paulo, São Paulo, Brazil

² Institute of Oceanography, University of São Paulo, São Paulo, Brazil

³ Department of Physical Oceanography and Meteorology, State University of Rio de Janeiro, Rio de Janeiro, Brazil

and adjacent oceanic areas (Rao et al. 1996; Zhou and Lau 1998; Gan et al. 2004; Vera et al. 2006; Garcia and Kayano 2009, 2013).

The SA rainy season commences over the northwest of the Amazon region (CAM) and extends to the Center-West (CWB) and Southeast (SEB) regions of Brazil in late September and early October. The mature phase occurs during the summer months (DJF), when the South Atlantic Convergence Zone (SACZ) becomes Brazil's primary active convective system (Kousky 1988; Rao et al. 1996; Gan et al. 2004; Vera et al. 2006; da Silva and de Carvalho 2007; Garcia and Kayano 2009; Carvalho and Cavalcanti 2016).

The SAMS has active and inactive phases during its life cycle. Gan et al. (2004) and Liebmann and Mechoso (2011) emphasize that the displacement of frontal systems from higher latitudes to the Southeast Brazil (SEB) region plays a crucial role in organizing SACZ-related convection and increasing precipitation in the monsoon region. Conversely, the absence of these systems during the rainy season leads to decreased rainfall, characterizing an inactive monsoon period. During the active monsoon phase (DJF), atmospheric circulation changes are associated with westerly wind anomalies from the northwest of the Amazon region (CAM) to the Southeast Brazil (SEB).

This factor directly influences the position of the Low-Level Jet (LLJ), enhancing the jet's intensity from the western Amazon towards Southeast Brazil (SEB). Additionally, intra-seasonal variability, such as the Madden–Julian Oscillation (MJO), affects the intensity of rainfall periods over the monsoon region. The SACZ and its spatial–temporal variability play a crucial role in defining the intensity of the rainy season in SEB and the Center-West (CWB) (Rao et al. 1996; Jones and Carvalho 2002; Gan et al. 2004; Carvalho et al. 2011, 2016).

The SACZ is characterized as a band of deep convection oriented in the Northwest–Southeast direction, extending from the Amazon region to the oceanic area adjacent to Southeast Brazil (SEB) (Kodama 1992, 1993; Zhou and Lau 1998; Liebmann et al. 2001; Carvalho et al. 2002, 2004; Marengo et al. 2012). According to Carvalho et al. (2004), the SACZ can be considered independent of its extension over the ocean, and intense convective activity may occur over the oceanic and Southeast Brazil (SEB) regions, regardless of what happens inland. Additionally, the convective activity associated with the oceanic cloud band may be triggered by the propagation of mid-latitude wave trains linked to the intraseasonal tropical oscillation, primarily the Madden–Julian Oscillation (MJO). Active SACZ-related rain exhibits a "seesaw" pattern, in which events with intense (weak) SACZ convective activity are associated with a deficit (abundance) of precipitation over the subtropical plains of South America. The precipitation response observed in the southern region of Brazil is related to the asymmetry

of the heat source associated with the SACZ, favoring the appearance of the subsidence branch of the circulation over the area (Casarin and Kousky 1986; Nogués-Paegle and Mo 1997; Gandu and Silva Dias 1998).

Significant changes in the SACZ positioning have been observed recently. For instance, Zilli et al. (2019) demonstrate that the difference in the mean state of the atmosphere between 2005 and 2014 led to a southward shift of the SACZ. This displacement is associated with changes in the spatial pattern of warming over the tropics in recent years, which alter the sea-level pressure gradient and land–ocean temperature contrasts. Concurrently, the South Atlantic Subtropical High intensifies and expands, causing the reduction (increase) of the dynamic component of the equatorial (polar) circulation margin of the SACZ, resulting in favorable conditions for the southward displacement of the convective zone. Several studies have indicated that SACZ variability may be related to changes in the South Atlantic Dipole pattern and intra-seasonal variability (Robertson and Mechoso 2000; Barros et al. 2000; Wainer and Venegas 2002; Carvalho et al. 2004; Chaves 2004; Talento and Barreiro 2012, 2018; Jorgetti et al. 2014; Vera et al. 2018).

In the paleoclimate context, several studies using proxies explore the monsoon system's variability since the Last Glacial Maximum (LGM) period. For example, Novello et al. (2017), in their examination of speleothems in the Jaraguá cave (located in Mato Grosso do Sul, Central Brazil), emphasize that the variability observed in the proxies indicates a wetter condition during the last glacial period (17,800–27,970 before the 1950's present/BP) when compared to the early and mid-Holocene (MH; 5,550–11,000 BP). Additionally, the authors demonstrate that the Early to mid-Holocene period was drier, associated with the decrease in summer insolation in the Southern Hemisphere (SH) during these periods.

Gorenstein et al. (2022) made a reconstruction compiling 173 paleoclimatic data from different sources (speleothems; marine, lacustrine, and terrestrial sediments; and soil samples) in SA during the mid-Holocene (MH; defined by the authors as between 7000- and 5000-years BP). The authors found that there was agreement between the different types of climate proxies. It was observed that there was a reduced rainfall in Amazonia, with the SA southern region becoming warmer and drier during the MH. On the other hand, the SAMS main core shows rainfall patterns below those observed in the pre-industrial period, due to weakening and a northward displacement of SACZ during the MH.

TraCE-21k simulations have been extensively studied, and their results have been validated in several studies using reconstructions of paleoclimatic records for the different periods encompassed in the last 21,000 years (Liu et al. 2009, 2012; Mohtadi et al. 2016; Wen et al. 2016; He et al. 2021), including identifying rainfall variability over South

America and SST variations in the South Atlantic Ocean (Marson et al. 2014; Wainer et al. 2015, 2021; Venancio et al. 2020; Aguiar et al. 2020; Santos et al. 2022).

The ocean freshwater flow is one of the main factors explaining the observed changes since the LGM. Marson et al. (2014) used the transient simulations of the TraCE-21k model to study the related impacts of the freshwater forcing on the changes in South Atlantic deep circulation during the last 21 ka. The authors showed that the freshwater flow in the model is an important factor in controlling the water column stratification, and consequently, the northward heat transport by the Atlantic meridional circulation. During the LGM, a density barrier prevented the NH dense waters from sinking, due to the presence of saltier Antarctic bottom waters than today. The current structure of the Atlantic meridional circulation was only achieved during the MH, due to deglaciation, after Heinrich Stadial 1 (H1; 19–14.64 ka BP), and the consequent decrease in salt concentrations in the deep waters.

Aguiar et al. (2020) studied how the early Holocene freshwater flow impacts on the SAMS using proxies and paleoclimatic simulations. The authors found SAMS strengthening, and sea surface temperatures (SST) changes due to the weakening of the South Atlantic Subtropical Dipole (SASD). The SAMS strengthening corresponds to 50% of the SA precipitation variation during the Early Holocene, and the changes of the SASD represent 31% of the SST variance in the South Atlantic Ocean. Furthermore, the authors also suggest that the more intense SAMS in the early Holocene is consistent with the weakening of the observed southeast trade winds due to freshwater flow.

The main objective of this study is to characterize the South American Monsoon System/SAMS during the last 21,000 years, focusing on the changes in the precipitation patterns and displacement of the South Atlantic Convergence Zone/SACZ and the Intertropical Convergence Zone/ITCZ. The data for the SAMS analysis is derived from a transient climate model simulation since the last glacial Maximum (LGM) provided by long integrations made by the NCAR-TraCE-21k—Transient Climate Evolution over the last 21,000 years (He 2011). The specific objectives of this study are to evaluate the SAMS, aiming the identification

of the main variability patterns during the past 21 ka, as well as the possible influences of climatic forcings, such as freshwater flow, orbital, ice cover, and greenhouse gases. The focus is on the following scientific questions:

1. How does the spatial and temporal variability of the LISAM mode changes in each subperiod (using the Walker et al. 2019 definition) of the 21,000 years?
2. What is the role of each individual climatic forcing in driving SAMS?
3. How the multidecadal and millennial variability changes over the last 21 ka?

2 Data and methodology

2.1 Data

TraCE-21k (He 2011) tropospheric decennial precipitation and low levels data such as temperature, specific humidity, zonal wind, meridional wind, and pressure at mean sea level were used. TraCE-21k is based on the National Center for Atmospheric Research's coupled earth system model, the Community Climate System Model version 3 (NCAR-CCSM3), with a spatial resolution of approximately 3.75°. The primary simulation (TraCE-21k FULL) starts from the Last Glacial Maximum (LGM) period to the pre-industrial period (PI). The model is forced by freshwater inflow into the ocean at specific periods and locations described in He (2011) and LGM proxies reconstructions obtained by Otto-Bliesner et al. (2006), changes in the orbital parameters of the last 21 ka to calculate the total solar flux (Berger 1978). In addition, Joos and Spahni (2008) described the concentrations of greenhouse gases in the simulations.

Data produced by four other TraCE-21k experiments called *single forcing* were also used, which separately consider Northern Hemisphere freshwater flow forcings (MWF), ice sheet height (ICE), orbital parameters (ORB), and greenhouse gases (GHG), as indicated in Table 1. Such simulations were used to explore each forcing type's impacts on past observed changes.

Table 1 TraCE-21k simulations were used; transient forcing; constant forcing; boundary conditions; and available period (HE 2011)

Models name	Transient forcing	Constant forcing and boundary conditions	Available period
Full TraCE-21k	All transients Forcings	—	22,000 years BP
TraCE-21k -MWF	Freshwater flow only in the Northern Hemisphere	Used state in 19 ka TraCE-21k	19,000 years BP
TraCE-21k -ICE	Ice sheet	Used state in 19 ka TraCE-21k	19,000 years BP
TraCE-21k -ORB	Orbital Parameters	Used state in 22 ka TraCE-21k	22,000 years BP
TraCE-21k -GHG	Greenhouse gases	Used state in 22 ka TraCE-21k	22,000 years BP

The Twentieth Century Reanalysis (R20C), prepared by the National Oceanic and Atmospheric Administration Climate (NOAA-CIRES-DOE) and made available via the NOAA Physical Sciences Laboratory (NOAA-PSL) (Compo et al. 2011), with 1° of spatial resolution, was used to determine the SMAS variability patterns during the instrumental period. All the meteorological variables used have a monthly temporal resolution.

In addition, observed monthly precipitation climatology data from the Global Precipitation Climatology Project (GPCP), with 2.5 degree of spatial resolution, made available by NOAA-PSL, were also used to compare with TraCE-21k precipitation (Adler et al. 2016).

As a comparison with the TraCE-21k patterns, data from climatic proxies from stalagmites spread across the SAMS regions in Brazil were selected as shown in Table 2.

2.2 Methodology

The Large Scale South American Monsoon Index (LISAM), developed by Silva and Carvalho (2007), was used to identify the evolution of the patterns corresponding to the SAMS and the SACZ. LISAM consists of a multivariate principal component analysis (EOF), combining surface precipitation (PREC) and low-level variables: temperature (TEMP), specific humidity (SHUM), zonal (UWND), and meridional (VWND) wind. To reproduce the same patterns that Silva and Carvalho (2007) identified, the variables were normalized by subtracting the mean and dividing by the standard deviation. The annual climatological cycle was removed.

The first EOF mode represents the SAMS, and the second mode is related to the SACZ. Spatial patterns were generated based on the linear correlation between the time series of the LISAM mode and the input analysis variables. The EOFs and the correlation patterns are shown here with a positive sign for the precipitation anomaly over the monsoon region.

The definition of the periods considered for the analysis of the last 21,000 years was based on the work of Marson

et al. (2014) and Walker et al. (2019), as described in Table 3.

R20C and GPCP were also used to compare the representativeness in TraCE-21k of the main meteorological systems in South America during the austral summer (December–January–February), as shown by the average precipitation rate in Fig. 1. In general, the TraCE-21k model (Fig. 1a) represents the monsoonal precipitation during the summer reasonably well, despite the intensity of rainfall being lower, with the band of the Intertropical Convergence Zone (ITCZ) predominantly in the Northern Hemisphere (NH), as presented for the instrumental period (Fig. 1b, c). In addition, the precipitation band associated with the SACZ is also reasonably reproduced, extending to the Atlantic Ocean region adjacent to the Southeast region of Brazil.

3 Results and discussions

3.1 The TraCE-21k Full Forcing monsoon

Silva and Carvalho (2007) described that the first variability mode (EOF1), shows positive precipitation anomalies throughout the monsoon region, extending towards the Atlantic Ocean adjacent to the SEB, with slightly negative

Table 3 The separation of different periods within the last 21,000 years is based on Marson et al. (2014) and Walker et al. (2019)

Periods	Years (ka BP)
Heinrich Stadial 1 (H1)	19.00–14.64
Bølling–Allerød (BA)	14.67–13.00
Younger Dryas (YD)	12.90–11.70
Early Holocene (EH)	11.70–8.2
Middle Holocene (MH)	8.2–4.2
Late Holocene (LH)	4.2–0.0

The years are in the unit of a thousand years before the 1950s present (ka BP)

Table 2 Paleoclimatic records

Proxies	Location	Stalagmites	References
Botuverá (BOT)	27.22° S, 49.15° O	BT2, BTV21a	Bernal et al. (2016), Cruz et al. (2005, 2007) and Novello et al. (2021)
Jaraguá (JAR)	21.08° S, 56.58° O	JAR2, JAR7, JAR14	Novello et al. (2019)
Lapa Sem Fim (LSF)	16.15° S, 44.60° O	LSF19, LSF15, LSF3	Azevedo et al. (2021); Strikis et al. (2018)
Lapa Grande (LG)	14.37° S, 44.28° O	LG3, LG11	Azevedo et al. (2021); Strikis et al. (2011); Strikis et al., (2018)
Paixão (PAI)	12.65° S, 41.05° O	PX7	Strikis et al. (2015, 2018)
Rainha (RAI)	05.60° S, 37.73° O	RN1	Cruz et al. (2009) and Utida et al. (2020)
Paraíso (PAR)	04.07° S, 55.45° O	PAR1, PAR3, PAR16, PAR7	Novello et al. (2021) and Wang et al. (2017)

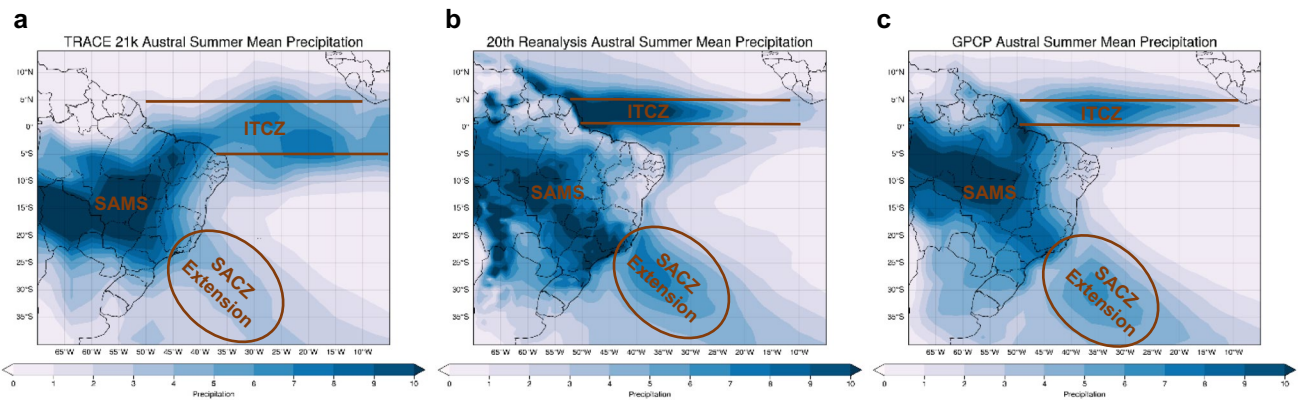


Fig. 1 Average precipitation rate during austral summer (December–January–February) for: **a** the last 1000 years of TraCE-21k; **b** average between 1836 and 2015 of the 20th-century Reanalysis; **c** the long-

term average of the GPCP between 1981 and 2010. The main location for ITCZ, SACZ and SAMS are also shown

anomalies near the extreme south of Brazil coast. Similarly, the second variability mode (EOF2), represents the oceanic portion of the South Atlantic Convergence Zone (SACZ). The oceanic SACZ is also influenced by the incursions of frontal systems, which represent one of the main catalysts for the organization of the SACZ convective structure. Thus, depending on the time scale, EOF2 can be interpreted as the pattern of the oceanic SACZ and frontal system incursions. EOF1 represents the pattern associated with the South American Monsoon System (SAMS) and the continental SACZ (Carvalho et al. 2002, 2004). Both patterns are similar to those found using the R20C (Fig. 2a, b, respectively).

3.1.1 Analysis of the entire 21 ka period

Figure 2 also shows the SAMS variability modes (LISAM/EOF1 and SACZ/EOF2) over the last 21,000 years. The pattern shown in EOF1 (Fig. 2c), which represents 58.6% of the total variance, is associated with the most intense rainfall over the Amazon Basin (CAM) region and has a northwest-southeast orientation towards the south and SEB. EOF2 (15.3% of the total variance) is characterized by a north/south dipole in the precipitation anomaly and shows the southeastward extension of the convective band over the South Atlantic (Fig. 2d). The 3rd EOF explains only 8.5% of the total variance and it is not shown in Fig. 2.

Differently from what is observed in the R20C period, the EOF1 pattern in TRACE21k reveals that the summer period precipitation variability is shifted southward compared to the R20C period (Fig. 2a), resulting in negative precipitation anomalies over the NEB region, Minas Gerais, and Goiás. The EOF1 time series (Fig. 3) shows that during the recent Holocene, the time series is positive, and the spatial pattern

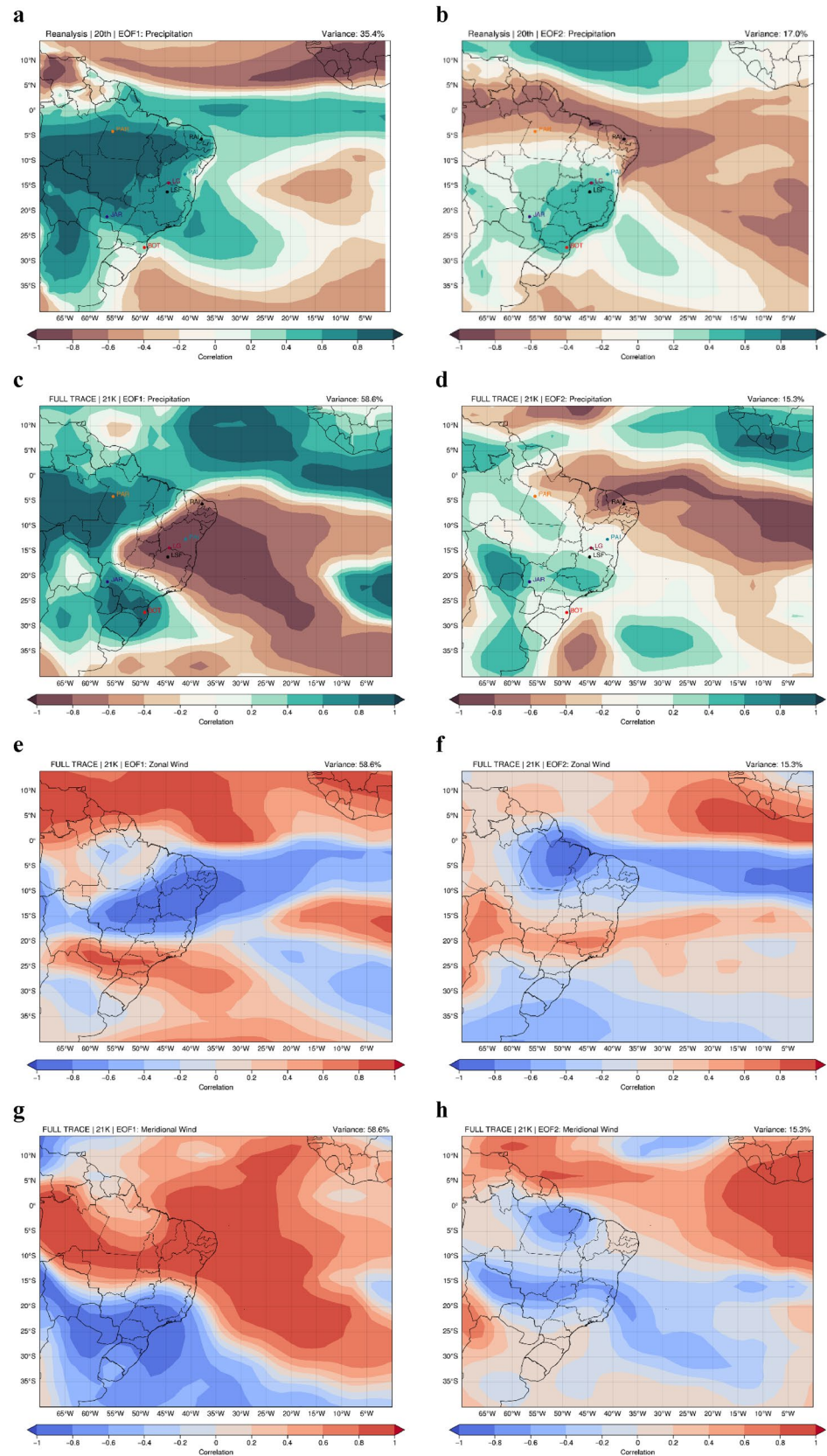
tends to have a greater weight in the current region of activity of the South Atlantic Convergence Zone.

The EOF time series was used to compare with climatic proxies across Brazil (Fig. 3). In general, the climatic transitions identified by the proxies between H1 and YD are well-defined, as shown in the records of “Lapa Sem Fim/LSF” (Fig. 3b) and “Jaraguá/JAR” caves (Fig. 3e). The TRACE21k simulation was able to identify the main changes in SAMS during the last 21,000 years, reasonably representing the variations found by the proxies in the main paleoclimatic periods studied, such as the anti-phase relationship of the EOF1 (blue line in Fig. 3a) and EOF2 (red line in Fig. 3a) time series with the proxies in the NEB region during the H1 and YD period (Fig. 3b, d, f and h).

For the H1 subperiod, the EOF1 time series is correlated in phase with the Paraiso/PAR (Fig. 3g) and Rainha/RAI (Fig. 3h) records, while LSF, Botuverá/BOT, Paixão/PAI, and JAR caves (Fig. 3b–f) are in anti-phase. In particular, the BOT (Fig. 3c) records show an anti-phase pattern in H1 compared to the EOF1 time series, although the spatial pattern of the mode indicates positive precipitation anomalies in the cave region. This can be explained due to a possible spatial pattern displacement in the TraCE-21k simulations compared to the observations since the same anti-phase pattern is also observed in JAR cave (Fig. 3e) for the H1 and YD. On the other hand, this difference can also be explained due to the degree of change recorded by the caves, with BOT (around 2‰) showing a lower degree of change than JAR (around 4‰).

Ward et al. (2019) show that the differences between the different climatic proxies over the monsoon region are also related to the local humidity pattern during the last 10,000 years. The authors emphasize that the main variability mode during this period follows the austral summer insolation variation due to the coupling with

Fig. 2 The spatial pattern was obtained with the correlation between the EOF expansion coefficients' time series, and the variables studied during the R20C and last 21,000 years. The first (second) column refers to the spatial patterns found with the first (second) mode of EOF1 (EOF2) for the variables: **a, b** R20C Precipitation; and, for the last 21 ka: **c, d** precipitation; **e, f** Zonal wind; **g, h** Meridional wind. It is also shown the location of the proxies of the caves of Botuverá (BOT), Jaraguá (JAR), Lapa Sem Fim (LSF), Lapa Grande (LG), Paixão (PAI), Rainha (RAI) and Paraíso (PAR) in the precipitation patterns (**a–d**)



the variations of the orbital parameters. Despite this, the proxies' highest correlation with this mode is in the Andean region and Atlantic Coast, also observed with the in-phase relationship between the EOF1 and EOF2 time series (Fig. 3a) with the BOT record (Fig. 3c) during the Holocene. On the other hand, some inland records, such as the Amazon region and the JAR cave, have different mechanisms intrinsically linked to the local humidity variation and in-cave conditions and not only to the regional variation of the South American monsoon. Thus, the variability presented by paleoclimatic records in the SAMS region demonstrates greater spatial and temporal heterogeneity due to humidity conditions and variations in the monsoon system itself (Bernal et al. 2016; Wortham et al. 2017; Ward et al. 2019; Gorenstein et al. 2022).

The regional role of the local moisture conditions is also observed in the recent historical period. For example, Garcia and Kayano (2015) and later Garcia et al. (2017) demonstrated that during the 1958–2014 period, subareas within the SAMS region showed differences in heat and water balances during the year. In particular, the authors studied the CAM and CWB regions, indicating that the CAM region acts predominantly as a source of moisture and heat during all months of the year, regardless

of the PDO phase. The CWB region, on the other hand, presented a well-defined variation as a sink (source) of moisture and a source (sink) of heat during the wet (dry) season.

In conclusion, the differences between the climate variability derived from proxies and the time series of LISAM and SACZ (main SAMS precipitation variability patterns) are compatible with the potential role of local humidity patterns and/or minor displacement of areas in the EOFs where their respective signs change in a short distance. The use of EOF analysis to detect the large-scale patterns associated with the SAMS variability is shown to be a useful analysis tool, the method has also been applied to paleoclimatic data for the last two millennia period in previous studies (Novello et al. 2021; Orrison et al. 2022). Furthermore, the EOF expansion coefficients time series can identify the main changes and temporal variability associated with the SAMS (Silva and Carvalho 2007). The LISAM mode identifies the patterns of larger total variability explained in the complete 21 ka period (up to 58.6%).

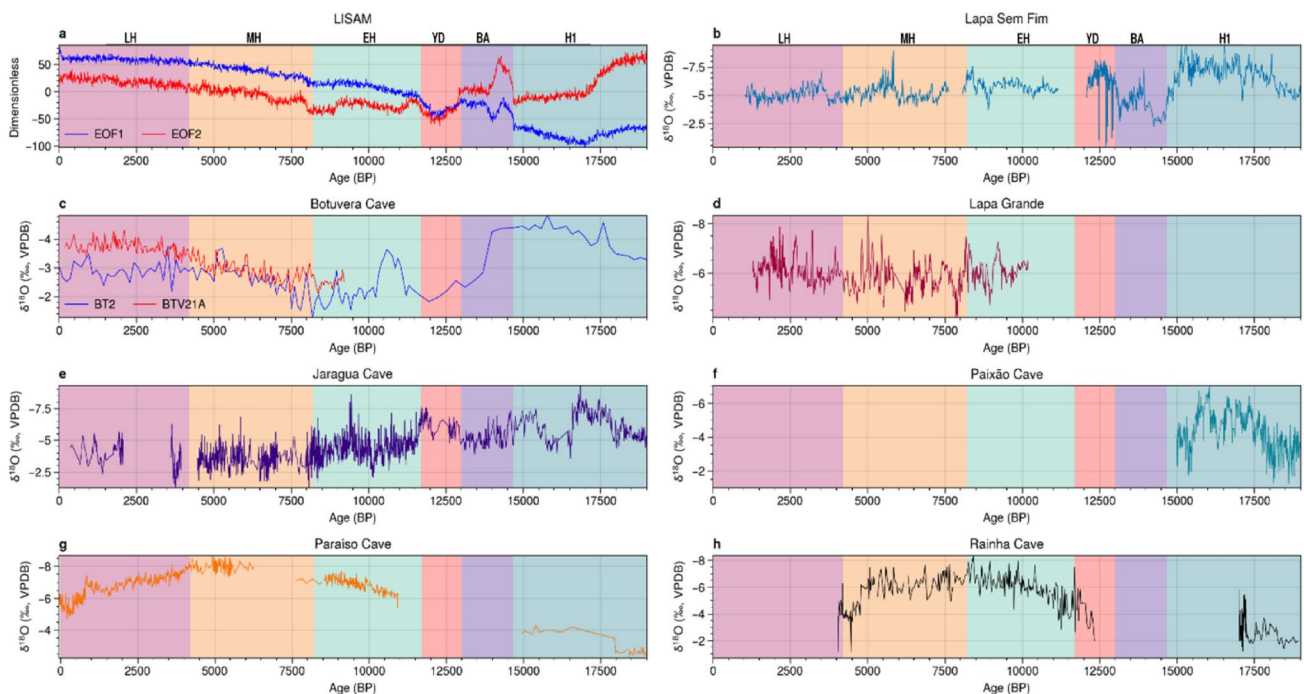
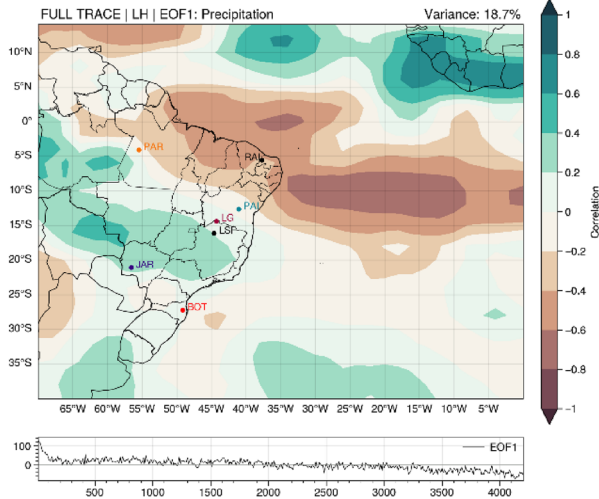


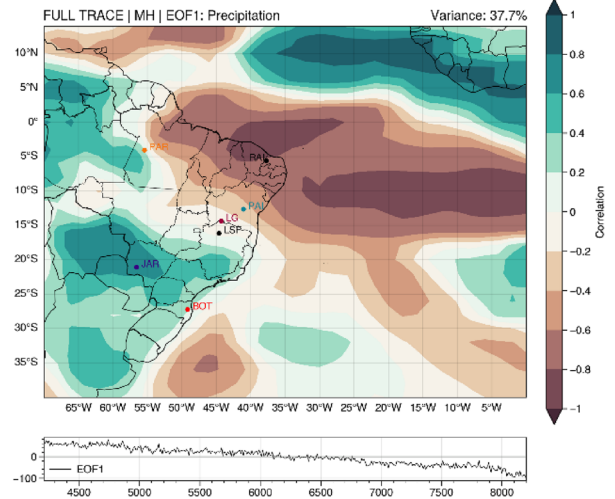
Fig. 3 Comparison between the time series of the EOF1 (blue line) and EOF2 (red line) expansion coefficients modes (a), with the $\delta^{18}\text{O}$ isotopic variation of the caves: **b** Lapa Sem Fim (LSF19+LSF15+LSF3; Azevedo et al. 2021; Stríkis et al. 2015, 2018); **c** Botuvera (Cruz et al. 2009); **d** Lapa Grande (LG3+LG11; Azevedo et al. 2021; Stríkis et al. 2011; Stríkis et al. 2018); **e** Jaraguá

(JAR2+JAR7+JAR14; Novello et al. 2019); **f** Paixão (Stríkis et al. 2015, 2018); **g** Paraíso (PAR1+PAR3+PAR16+PAR7; Novello et al. 2021; Wang et al. 2017); **h** Rainha (Cruz et al. 2009; Utida et al. 2020). *LH* Late Holocene; *MH* Middle Holocene; *EH* Early Holocene; *YD* Younger Dryas; *BA* Bølling–Allerød; *HI* Heinrich Stadial 1

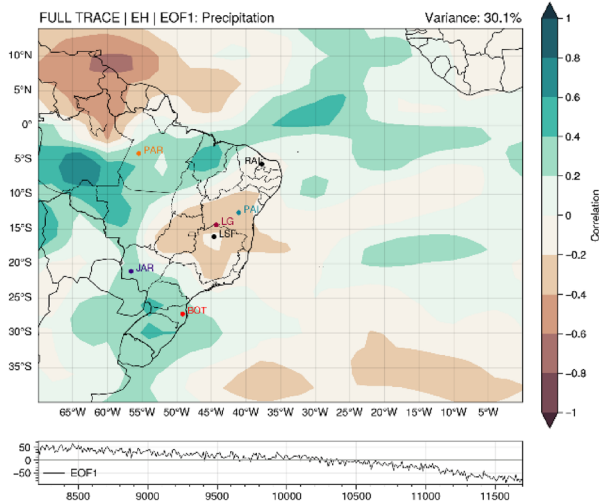
a



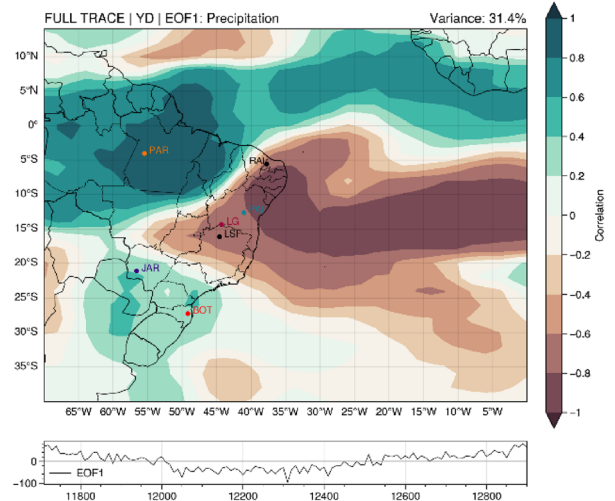
b



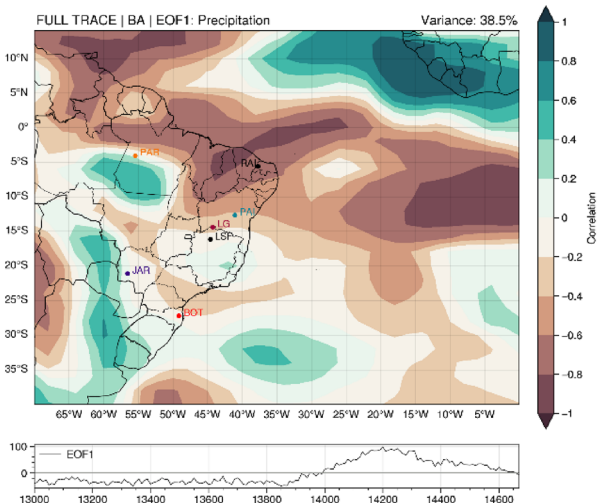
c



d



e



f

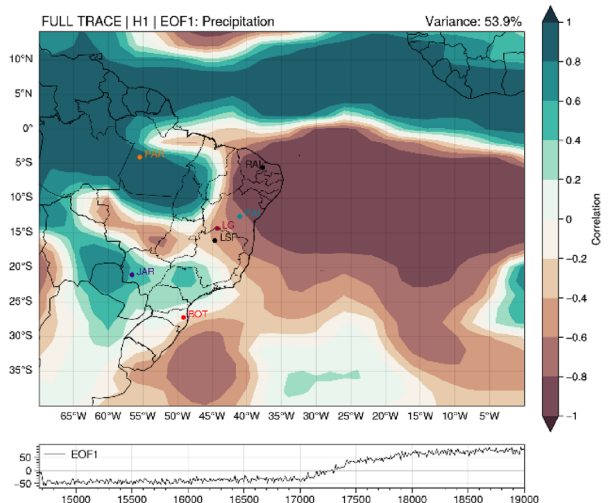


Fig. 4 Spatial patterns and time series of the expansion coefficients of the first variability mode of LISAM applied in TraCE-21k Full Forcing in the precipitation variable, subdivided into the periods: **a** Late Holocene (LH); **b** Middle Holocene (MH); **c** Early Holocene (EH); **d** Younger Dryas (YD); **e** Bølling–Allerød (BA); **f** Heinrich Stadial 1 (H1). It also shows the location of the climatic proxies of the caves of: *BOT* Botuverá, *JAR* Jaraguá, *LSF* Lapa Sem Fim, *LG* Lapa Grande, *PAI* Paixão, *RAI* Rainha, *PAR* Paraíso

3.1.2 Monsoon patterns in the 21 ka subperiods

The EOF analysis was applied separately for each subperiod of the last 21 k (Table 3) to explore SAMS changes. Figures 4 and 5 compare the precipitation spatial patterns obtained in each subperiod for EOF1 and EOF2. As shown in Fig. 4, the SAMS precipitation varied considerably among the subperiods, with explained variances ranging from 18.7% (LH) (Fig. 4a) to 53.9% (H1) (Fig. 4f).

Marson et al. (2014) show that the MWF predicted in the model simulation is present mainly between 5 and 19 ka BP, with the bulk of the freshwater flow in the NH. In the SH, there is only one large pulse, which is the globally most intense (60 m/ka), around 14 ka BP. The LH period (Fig. 4a) is the only subperiod with no MWF forcing. The BA period is the only one that it is influenced by the SH freshwater pulse. The SH is influenced by just another pulse, with very small magnitude (1 m/ka) between 12 and 5 ka (EH–MH).

Regarding the BA subperiod (Fig. 4e), it is noteworthy that the precipitation pattern of EOF1 differs from the first pattern observed in the other subperiods and the entire period (Fig. 3). In fact, EOF1 and EOF2 exhibit inverted spatial structures, meaning that the first mode, which explains most of the variance, is not similar to LISAM, which appears as the second mode (Fig. 5e). The BA is characterized by a sudden warming due to abrupt climatic changes associated with variations in the Atlantic Meridional Circulation (AMOC) intensity, consistent with findings in paleoclimatic records (Liu et al. 2009).

The intensification of AMOC during the BA occurs despite the strong freshwater pulse in the NH, which would typically weaken the meridional oceanic circulation (Liu et al. 2009, 2015; Obase and Abe-Ouchi 2019). However, Obase and Abe-Ouchi (2019) suggest that this strong warming was also a response to the presence of meltwater from the continental ice sheet. With more significant warming in the NH during the BA, the ITCZ tends to shift further north to balance atmospheric heat transport (McGee et al. 2014, 2018; Marshall et al. 2014; Schneider 2017; Lutsko et al. 2019).

EOF1 in the BA period (Fig. 4e) shows that most of the explained precipitation variance is associated with changes in the ITCZ position (Hughen et al. 1996; Liu et al. 2009; Deplazes et al. 2013; Mulitza et al. 2017). In fact, Fig. 4e shows positive precipitation anomalies concentrated in the

North Atlantic near Africa, while negative anomalies predominate in practically the entire Tropical Atlantic. EOF2 (Fig. 5e) represents the SAMS pattern during the subperiod, with positive precipitation anomalies over the ITCZ region, extending to the CAM region and towards southern Brazil.

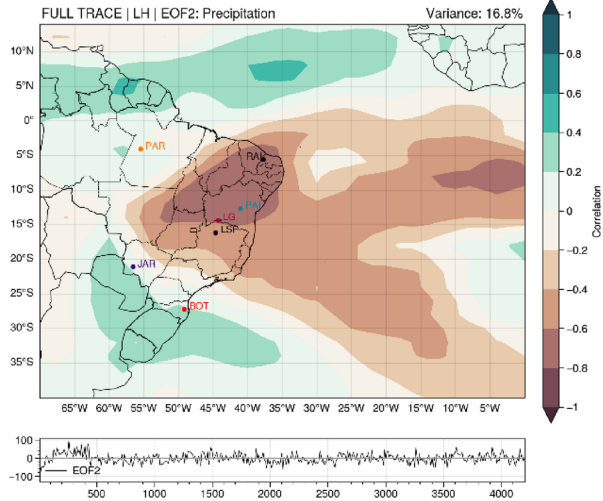
The H1 (Figs. 4f and 5f) and YD (Figs. 4d and 5d) periods are colder, with the highest MWF in the NH. These periods are also associated with AMOC weakening (McGee et al. 2014) and, consequently, a southward shift of the ITCZ (McGee et al. 2014, 2018; Moreno-Chamarro et al. 2020). In this way, the SAMS pattern for both subperiods is similar to that found for the complete 21,000 years period (Fig. 3). Differences with respect to the EOFs for the entire 21 k period are observed in the southern region of Brazil during the H1, with the anomalies shifting to southeast of Brazil due to the north wind anomalies (Fig. 4g) over Uruguay and the southernmost part of Brazil.

The ITCZ southern shift implies an increase in precipitation over NEB as observed in the precipitation spatial patterns (Figs. 4f and 4d) together with the EOF1 time series sign change at around 17.25 ka (H1) going from positive to negative in parts of the H1 and YD (12.50 ka). The LISAM time series sign reversal from positive to negative is associated with increased rainfall in the NEB. The TraCE-21k response is consistent with the NEB paleoclimatic records, with increased precipitation intensity appear in the proxies of the Lapa Sem Fim (Fig. 3b) and Paixão (Fig. 3f) caves.

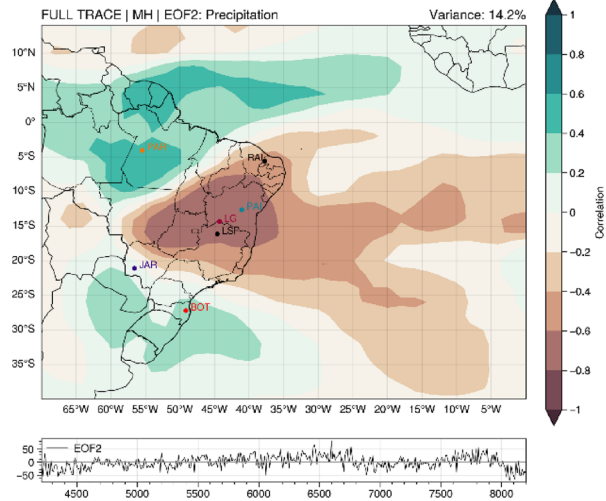
The TraCE-21k precipitation increase in the CAM region is also related to the ITCZ southward shift. Furthermore, the changes in the atmospheric circulation, with more intense trade winds from the north towards NEB and northern region of Brazil (McGee et al. 2018), causes the LLJ to change direction and shift towards the south, corroborating the pattern found in the H1 and YD. Both H1 (Fig. S2f) and YD (Fig. S2d) are characterized by easterly wind anomalies over the NEB region and continuing towards the CWB. Concomitantly, the EOF1 wind anomalies are westerly over the northern region, SEB and southern Brazil, indicating a southward wind pattern shift. Although both H1 and YD subperiods show ITCZ southward displacement, the YD (Fig. 4d) shows a stronger precipitation positive anomaly pattern over southern Brazil, while in the H1 (Fig. 4f), the highest precipitation loading is in SEB and CAM regions.

It is important to note, as seen in the EOF1 time series (Fig. 4f), that the H1 analysis must be considered separately for two subperiods, the first between 19 ka and 17.5 ka BP and the second between 17.23 ka and 14.68 ka BP, here called H1a and H1b, respectively, due to the reversal of the LISAM time series signal. The prevailing positive anomalies, shown in Fig. 4f, persists in H1a, mainly as a response to the SAMS intensification due to deglaciation and AMOC reduction (Mulitza et al. 2017).

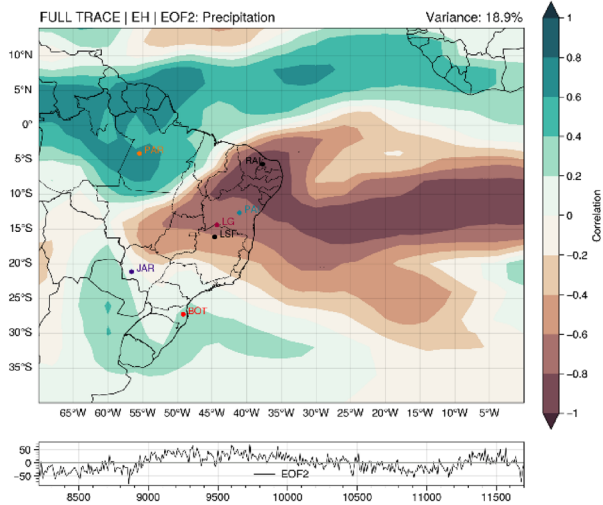
a



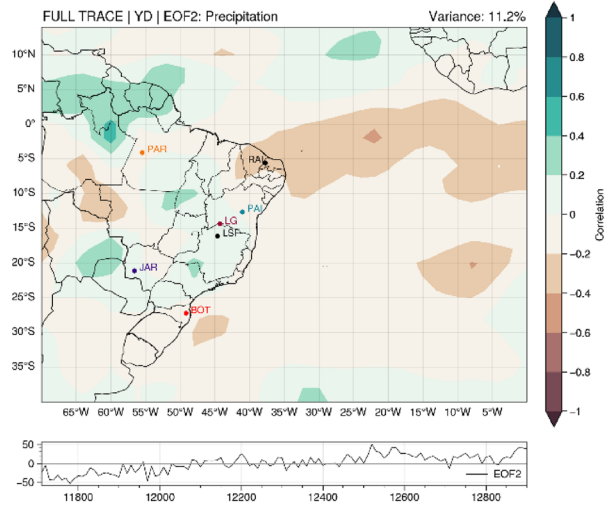
b



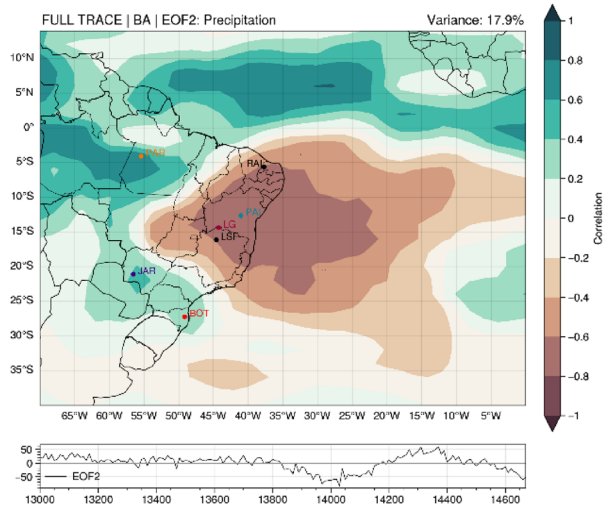
c



d



e



f

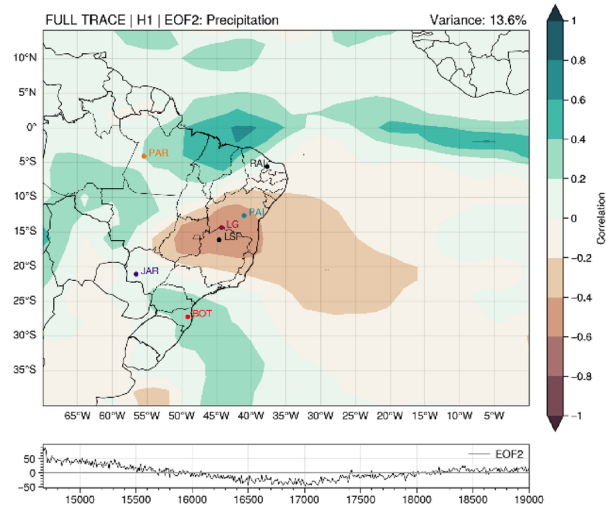


Fig. 5 Spatial patterns and time series of the expansion coefficients of the second variability mode of LISAM applied in TraCE-21k Full Forcing in the precipitation variable, subdivided into the periods: **a** Late Holocene (LH); **b** Middle Holocene (MH); **c** Early Holocene (EH); **d** Younger Dryas (YD); **e** Bølling–Allerød (BA); **f** Heinrich Stadial 1 (H1). It also shows the location of the climatic proxies of the caves of: *BOT* Botuverá, *JAR* Jaraguá, *LSF* Lapa Sem Fim, *LG* Lapa Grande, *PAI* Paixão, *RAI* Rainha, *PAR* Paraíso

However, EOF1 amplitude decreases from 17.23 ka BP, causing the precipitation anomalies over the NEB region to increase and, consequently, a rainfall shifts from the SEB. The precipitation changes during the H1 are consistent with the Stríkis et al. (2015) proxy-based analysis. The rainfall regime in this period was called by the authors as the “mega-SACZ”, due to the coincidence of the southward ITCZ shift and the SACZ northward shift. The YD shows the same behavior (Fig. 4d). In this case, the YD is characterized by EOF1 time series sign inversion between 12 and 12.6 ka BP. The NEB precipitation shift is related to the increase in the intensity and northward displacement of the oceanic SACZ,

Despite the EOF1 spatial similarity between the cold periods, H1 and YD, EOF2 pattern differs. The EOF2 (Fig. 5f) in H1 shows positive anomalies in the Tropical Atlantic (between 5° S and 5° N), consistent with the ITCZ southward shift, extending westward towards CAM and with positive precipitation anomalies in southern Brazil. In addition, the H1 EOF2 indicates negative precipitation anomalies over the central and NE Brazil.

Several studies show that under SST specific conditions, changes in the pressure gradient at sea level and the tropical warming contribute to the strengthening latitudinal shift of the SACZ and, consequently, the intensity of the SAMS rainy season (Wainer and Venegas 2002; Talento and Barreiro 2012, 2018; Jorgetti et al. 2014; Vera et al. 2018; Zilli et al. 2019). Jorgetti et al. (2014) highlight that northward shifted SACZ events are associated with negative SST anomalies under the convective band, extending along the SEB coast. The authors showed that the oceanic forcing into the atmosphere favors the SACZ northward shift due to the change in the atmospheric pressure pattern. In this same context, Bombardi et al. (2014) demonstrated that the SASD plays an essential role in the intensity and latitudinal shift of the SACZ. There is a larger probability of establishment of intense oceanic SACZ during the SASD negative phase, characterized by negative SST anomalies in the southwest pole and positive in the northeast.

Wainer et al. (2021) used the entire TraCE-21k period to study changes in the SASD. The authors conclude that the SASD pattern is in its positive phase (positive SST anomalies in the northeast pole and negative in the southwest pole) between 19 and 17 ka BP and negative between 17 ka and 14.5 ka BP. The precipitation anomalies increase in NEB during H1b (discussed above), related to the stronger and

northward shifted oceanic SACZ, is consistent with the patterns found by Wainer et al. (2021). In addition, the same behavior is observed in the YD, when the SASD signal is negative and most intense between 11.8 and 12.6 ka BP, influencing the NEB rainfall increase.

The positive and intense SASD phase during the BA also explains the reversal of the observed precipitation patterns between EOF1 and EOF2. Positive SASD phase implies colder anomalies in the tropical South Atlantic, causing the southward precipitation shift, associated to the second mode (Fig. 5e). In contrast, the first mode (Fig. 4e) represents the change in variability of tropical precipitation associated with the ITCZ’s northward displacement, also related to the tropical South Atlantic cooling (Liu et al. 2009; Obase and Abe-Ouchi 2019).

Another similar precipitation pattern found with the entire 21 ka period was identified in EH (Fig. 4c). EH is characterized as a period of climate transition, with the NH warming up again in response to the AMOC intensification (McGee et al. 2014). The spatial patterns found in EH are less intense than those found for the entire 21 k period. However, the EH precipitation pattern represent a resumption of the predominant precipitation pattern detected in the complete 21 ka, as shown by the period of sign reversal of the EOF1 time series. SASD phase continues to be negative during the beginning of the EH (Wainer et al. 2021) and acts as a stimulus for increased precipitation in NEB. However, from 10.5 ka BP on, the precipitation tends to weaken in NEB and increase over the monsoon region, related to the atmospheric response to warming of the NH and increasing AMOC intensity (McGee et al. 2014; Mulitza et al. 2017).

According to Wainer et al. (2021), the SASD pattern tends to weaken after 8 ka BP, with the time series changes to positive sign from 6 ka BP to the historical period. The SASD weakening also influences the beginning of the northward ITCZ migration, contributing to the reduced precipitation over NEB. Thus, from the EH on, the EOF1 time series indicates a stronger SAMS pattern (more positive) for the MH (Fig. 4b) and LH (Fig. 4a).

According to Donohoe et al. (2013) and McGee et al. (2014, 2018), the MH (Fig. 4b) is characterized by the northward ITCZ shift due to the North Atlantic warming and the increase in the AMOC northward heat transport, a pattern very similar to that observed in the modern period. Liu et al. (2017) highlight that the mechanism responsible for the ITCZ shift is caused by the increase of the NH monsoon intensity, which, in turn, intensifies the wind stress in the ocean, strengthening the oceanic gyre and the oceanic northward heat transport at the equator. That is, the atmosphere compensates for the enhanced oceanic heat transport by shifting the ITCZ to the NH, so that global heat transport comes into equilibrium.

Garcia and Kayano (2009, 2013) showed that in the recent historical period, the intensification of the NH monsoon might precede the intensification of the SAMS half a year later. In fact, the precipitation patterns associated with the LISAM mode (Fig. 4b) show that the prevailing precipitation anomalies during the MH are found in the CAM region with displacement towards SEB, with the ITCZ located around 10°N and closer to the African coast. Therefore, the TraCE-21k patterns agrees with the mechanisms described above and are consistent with the proxy studies (McGee et al. 2014, 2018).

As in the BA, the LH also shows inversion in spatial patterns of larger variability. EOF1 (Fig. 4a) represents the SACZ mode described by Silva and Carvalho (2009) and explains about 18.7% of the total variance. EOF2 (Fig. 5a) represents a pattern like the SAMS, with 16.8% explained variance. As stated before, the LH is the only subperiod that does not have any MWF in the TraCE-21k simulations. This fact led to the similarity of the SAMS EOFs variance. The EOF1 time series during the LH (Fig. 4a) shows that the associated spatial pattern has a strong tendency to intensify towards the recent historical period due to the orbital forcing as discussed in the next section.

3.2 Impacts of each single forcing on SAMS

To explore the impacts of individual forcings on SAMS variability modes, the TraCE-21k single forcing experiments are analyzed (described in Table 3). The same EOF analysis is now applied to each single forcing experiment.

Figure 6 shows the EOF1 and EOF2 spatial patterns for each single forcing experiment. For EOF1, in general, the single forcing experiment most similar to the FULL experiment (Fig. 6a) is the MWF (Fig. 6b). The ORB (Fig. 6c), GHG (Fig. 6d), and ICE (Fig. 6e) experiments indicate a southward shift of the monsoon precipitation when compared to the FULL experiment.

The influence of the individual forcing on the precipitation variability for the full 21 ka period is analyzed by the EOF1 spatial patterns and their respective standardized time series (Fig. 7a). The LISAM pattern is the 1st EOF for all single forcing experiments (Fig. 6a–e). EOF2 of the single forcing, on the other hand, shows more spatial and time variability compared to the FULL cased (Fig. 6f–j). For the entire 21 ka period, the correlations between the single forcing experiments and the FULL, in descending order, are GHG: 92.2%; ICE: 89.8%; MWF: 75.9%; ORB: 71.4%.

Wainer et al. (2021) highlight that the MWF experiment significantly impacts the SASD variability of the FULL experiment, especially in H1 and YD. As with SASD, the LISAM mode also shows a strong relationship between MWF and FULL experiments in H1 and YD, partially due

to the influence of the negative phase of SASD on SAMS intensity, during cold periods.

However, unlike SASD during the YD, the LISAM mode also shows the greenhouse gas emissions influence and the earth's orbital cycle change (with the sign reversal beginning at the EH) (Kutzbach et al. 1998). That is, the NH insolation decrease, together with the freshwater flow and the decline in greenhouse gases, play an essential role in the displacement of precipitation towards the NEB and as previously shown, in the southward migration of the ITCZ.

During H1a, LISAM shows changes consistent with those observed mainly in the ICE and GHG experiments. In fact, the influence of the GHG emission and the reduction of the ICE forcing is related to the deglaciation, causing the precipitation, at first, to respond directly to a decrease of the ice sheets, as well as lower emission of the greenhouse gases. However, the other individual forcings also influence SAMS during H1b. Freshwater flow from ice sheet melt, from 17 ka onward, as shown in Marson et al. (2014), begin to affect precipitation in SAMS because of the changing heat redistribution in the South Atlantic and directly impact the oceanic variability modes, such as SASD (Wainer et al. 2021). In general, although the freshwater pulses do not have the largest correlation over the entire period, the pulses are essential for the representativeness of the abrupt changes observed in SAMS during H1, YD, and BA and consistent with the proxy analysis (Fig. 5).

Contrary to the EOF1 behavior, for EOF2 (Figs. 6f–j and 7b) the orbital forcing controls the SAMS precipitation (60.5% correlation), followed by the ICE experiment (− 22.2% correlation), while the other experiments do not show significant correlations with the EOF2 time series. The EOF2 spatial patterns show that orbital parameters significantly influence the SACZ. The southward migration observed in the recent period (Fig. 2a) is mainly modulated by insolation. This is a feature common to both SAMS (EOF1) and the oceanic SACZ (EOF2) patterns, which correlate strongly with the increase in insolation observed from the MH.

3.3 Multidecadal and millennial variability

The continuous wavelet transform (with the Morlet wave function), with 95% significance level (solid lines in figures), was applied to the time series of the expansion coefficients of each mode in the complete 21 ka of each experiment (Table 3), to explore potential coherence in the multidecadal and millennial time scales of the LISAM and SACZ mode. Wavelet analysis was also computed for the FULL experiment described in Table 1. The results of the single forcing experiments for the TraCE-21k FULL variability are shown in Sect. 3.3.1. The variability results

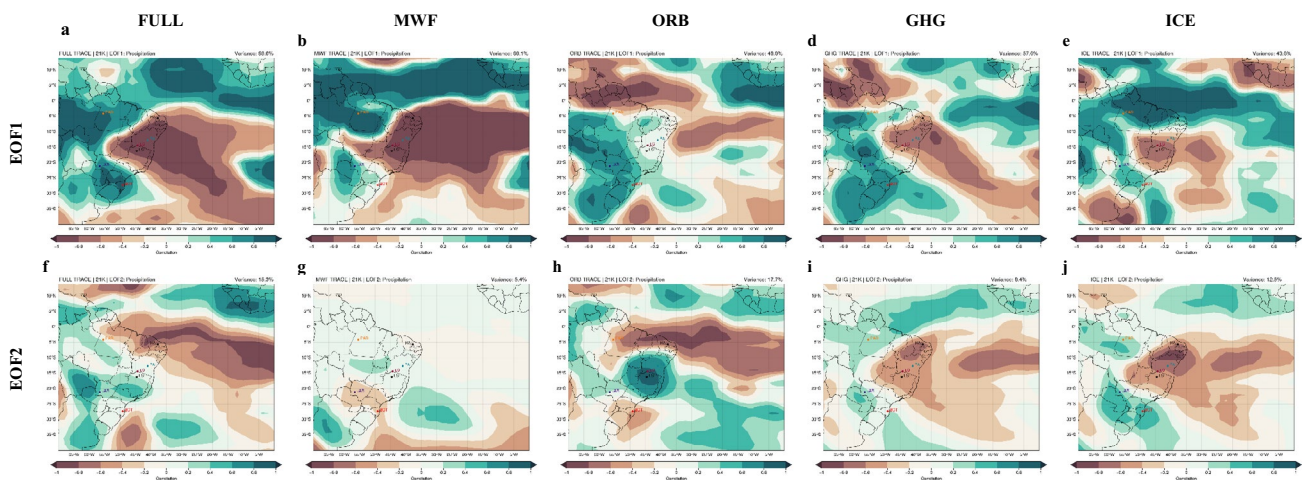
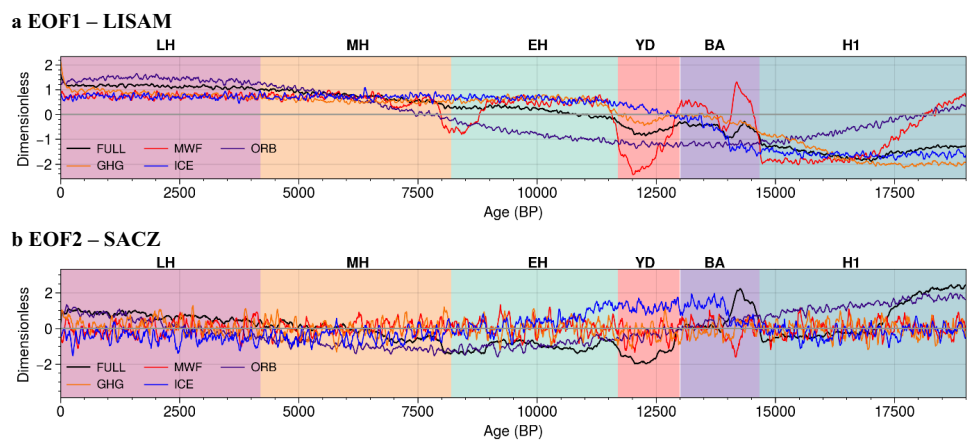


Fig. 6 Precipitation EOF1 (first line) and EOF2 (second line) spatial pattern applied in single forcings experiments of TraCE-21k, being: **a, f** Full Forcing (FULL); **b, g** Northern Hemisphere Freshwater Flow (MWF); **c, h** Orbital forcing (ORB); **d, i** Greenhouse gases (GHG); **e, j** Ice cover (ICE)

Fig. 7 Standardized and filtered (10-point moving average window) time series of the EOF1 (**a**) and EOF2 (**b**) expansion coefficients for the FULL (black), MWF (red), ORB (indigo), GHG (orange) and ICE (blue) experiments



applied in each of the subperiods (Table 3) are shown in Sect. 3.3.2.

3.3.1 Analysis for the single forcing experiments

The analysis shows a clear difference in the spectral energy peaks of the FULL (Fig. 8a) and MWF (Fig. 8b) experiments with the others at high frequencies, with the very little energy present in the modes with period less than 640 years. All experiments present most of the spectral power at lower frequencies (period above 2500 years). The highest spectral peak present in the FULL experiment (Fig. 8a) occurs mainly between H1 and EH, with periodicity varying between 640 and 5 ka, in addition to presenting energy on the multidecadal scale, but with a lower and significant intensity only at the 85% level. The same behavior is observed in the EOF2 wavelet analysis (Fig. 8f).

The lowest frequency spectral energy (corresponding to periods of the order of 640 to 5 ka) extends from 19 to 6 ka BP in the MWF case (Fig. 8b), coinciding with the end of freshwater pulses in the TraCE-21k simulation. In both experiments, the wavelet spectrum energy shifts to higher frequencies (period below 640 years), starting at 15 ka BP, coinciding with the BA freshwater flow events, revealing abrupt changes (Wainer et al. 2021) and showing a funnel shape in the wavelet spectrum. According to Addison (2018) and as discussed by Wainer et al. (2021), the funnel shape in the wavelet spectrum is a feature associated to significant signal discontinuities, which contributes to the energy leakage from lower to higher frequencies.

The GHG (Fig. 8d) and ICE (Fig. 8e) experiments also present energy peaks at the lower and predominant frequencies between the H1 and YD. This is another evidence of the melting ice and greenhouse gas emissions impact on the low-frequency variability of SAMS during cold events

in NH. In particular, the thaw influence also contributes to the high energy in the approximately 2 ka period during the BA, indicating the relationship with the NH heating, which caused accentuated ice sheet melting and, consequently, contributes to the GHG emission as well as the increased impact of GHG during the YD, as shown in Fig. 8d.

The GHG, ICE, MWF and ORB experiments show the highest energy peaks confined to the periods below 640 years, with the peak occurring mainly in the multi-decadal scale, from 30 to 80 years. This fact highlights the

Pacific Decadal Oscillation (PDO) and Atlantic Multidecadal Oscillation (AMO) importance in the precipitation associated with the oceanic SACZ. In fact, several studies show that the variability of the SACZ intensity and location is also influenced by the PDO and AMO (Mantua and Hare 2002; Carvalho et al. 2002, 2004; Chiang and Vimont 2004; Chiessi et al. 2009; Vuille et al. 2012; Novello et al. 2012, 2021; Apaéstegui et al. 2014; Carvalho and Cavalcanti 2016; Zilli et al. 2019).

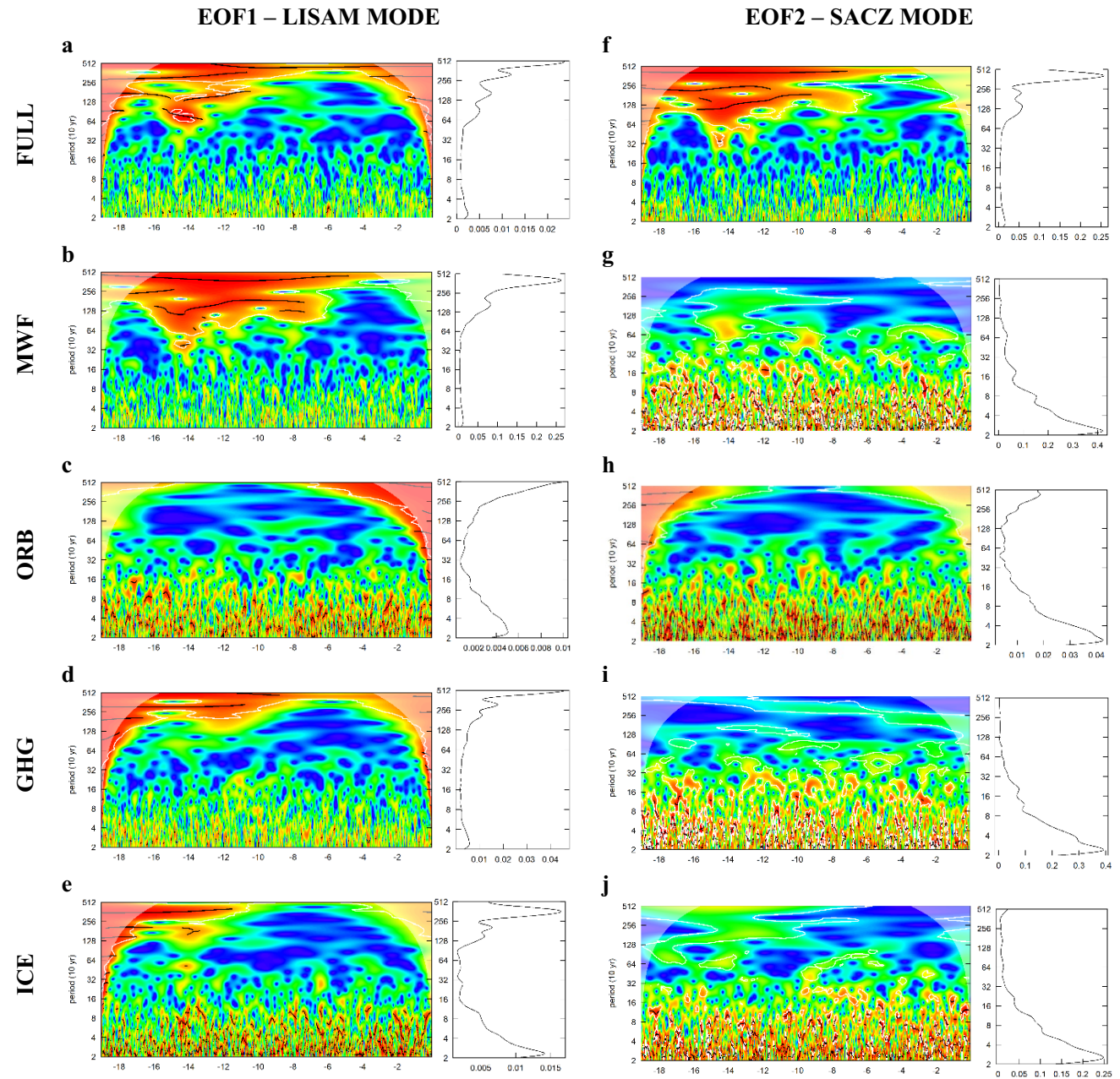


Fig. 8 Wavelet transforms applied to the EOF1 (first column) and EOF2 (second column) time series for the TraCE-21k experiments: **a, f** FULL; **b, g** MWF; **c, h** ORB; **d, i** GHG; **e, j** ICE. The black solid line in the spectrum shows the 95% significance level

In addition to the variabilities highlighted above, the period of variation of around 30 years in the FULL experiment is consistent with the multidecadal variability of the PDO and AMO, being influenced by orbital forcings (Fig. 8c) and by ice melting (Fig. 8e). Both experiments also show confined energy peaks with period under 160 years (Chen et al. 2021).

For the temporal variability of EOF2 (Fig. 8f–j), the FULL experiment presents the highest energy in low-frequency modes (periods around 5 ka), with the energy transfer to higher frequencies in the form of a funnel, as in the EOF1 case. The single experiment that shows significant energy in modes with period of the order of 5 ka is the ORB (Fig. 8h), confirming the influence of orbital forcings on the modulation of the position and intensity of the SACZ.

3.3.2 Analysis for 21 ka subperiods

The wavelet transform was applied to the time series of the expansion coefficients of the EOF1 and EOF2 (Fig. 9) patterns, obtained for each subperiod described in Table 3, to verify the changes in the variability modes of the FULL experiment during the entire 21,000 years. It is worth noting that, due to the smaller number of time samples, the YD (Fig. 9d, j) and the BA (Fig. 9e, k) present a smaller cone of influence of the wavelet analysis, being necessary to limit the analysis at the 1280 years period while the others go up to 2560 years.

Through the analysis of Fig. 9, it is immediately noticed that the multidecadal–centennial variability (below 320 years) has little energy in H1 (Fig. 9f, l) and BA (Fig. 9e, k), showing an increase in power as time advances towards the LH (Fig. 9a, g), mainly after the MH, and such periodicities are consistent with the main variability modes of the Pacific and Atlantic Oceans. In fact, Wainer et al. (2021) show that the SASD spatial pattern observed in the recent period initiates during the MH when the forced freshwater flow terminates in the simulations. In addition, the authors emphasize that MWF tends to make the South Atlantic warmer, contributing to the observed differences in the SASD variability from H1 to EH. Therefore, the end of freshwater discharges contributes to the formation of the oceanic variability observed in the recent period and to the increase in spectral energy present in the frequencies associated with multidecadal variability.

On the other hand, the opposite behavior in the energy spectrum is observed in low-frequency modes, with period above 1280 years, for both EOFs, showing a decrease toward the LH (Fig. 9a, g). As suggested earlier, the very low-frequency modes are intrinsically related to the orbital forcing, ice sheets, and freshwater flow. With the end of the MWF,

around 6 ka onwards, the energy associated with the MWF and ORB forcing tends to decrease in the more recent period.

Therefore, the SAMS and SACZ temporal variability are intrinsically related to MWF in past periods, with the energy of the decadal variability modes increasing from the MH, due to the end of freshwater flows, and the stabilization of oceanic patterns as observed in the recent period. In addition, orbital forcing also plays an essential role in modulating the SACZ multidecadal variability, contributing to the increase in the energy contained in the multidecadal modes of the TraCE-21k FULL experiment consistent with proxy-based studies (Chiessi et al. 2009).

4 Summary and conclusions

The main objective of this paper was to study the spatial and temporal variability of the South American Monsoon System (SAMS) and its structure during the last 21,000 years. We used the TraCE-21k experiments and validated the results against proxy-based studies. In addition, we aimed to analyze the precipitation variability in the H1, BA, YD, EH, MH and LH subperiods, and the influence of the individual climatic forcings (such as ice sheet melting, greenhouse gases, meltwater flux and orbital changes) on the spatial and temporal SAMS variability. The EOF analysis of the SAMS is based on Silva and Carvalho (2007) method which was applied to the TraCE-21k simulation results at decadal time scale. The EOF1 and EOF2 represents the main spatial patterns associated to the SAMS (LISAM and SACZ, respectively). Some highlights of the results follow.

The TraCE-21k EOF analysis compared to R20C and proxies:

For the entire 21,000-year period the SAMS and SACZ spatial pattern (Fig. 2c, d) are similar to the R20C's (Fig. 2a, b). For EOF1, the TraCE-21k differs from the R20C showing more concentrated precipitation in the Amazon Basin and a northwest-southeast orientation of the rainfall pattern towards the South and Southeast regions of Brazil. TraCE-21k EOF1 also presents negative precipitation anomalies, mainly over the NEB. There is a seesaw in the precipitation anomalies pattern between the Amazon Basin and the NEB that can be explained as a response associated with the Walker circulation induced by the Amazonian heat source. This pattern is related to the ITCZ shift that is associated with changes in Hadley cell intensity.

The time series of the TraCE-21k EOFs expansion coefficients (Fig. 3a) reveal the main changes in the SAMS precipitation inferred from the observed paleo-records (Fig. 3b–h), with differences that are consistent with the influences of local humidity in the region of each proxy or due to small changes in the spatial pattern in are with

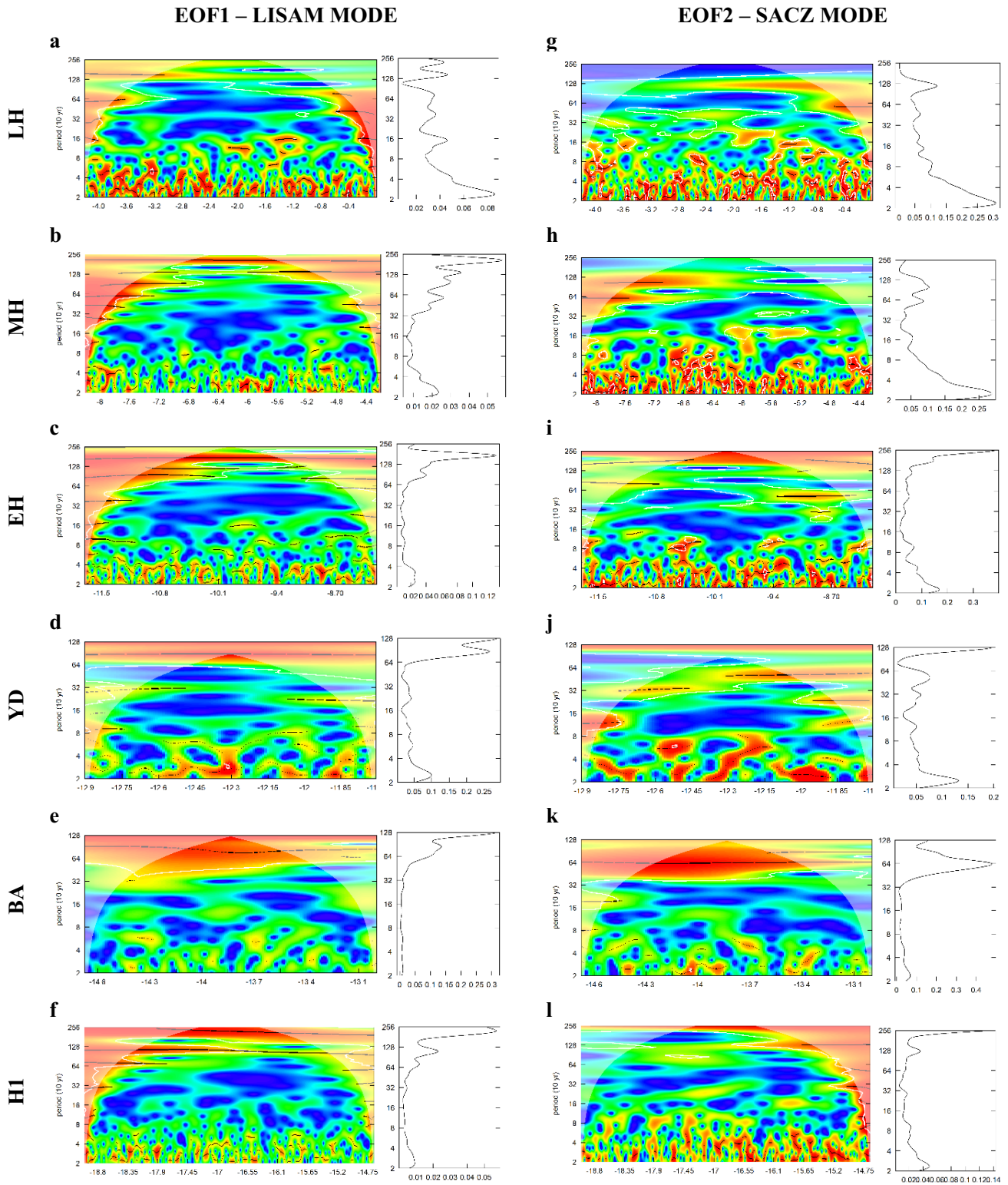


Fig. 9 Wavelet analysis applied in EOF1 (first column) and EOF2 (second column) for TraCE-21k FULL periods, as follows: **a, g** LH; **b, h** MH; **c, i** EH; **d, j** YD; **e, k** BA; **f, l** HI. The black solid line in the spectrum shows the 95% significance level

sharp gradients. Furthermore, as discussed by Gorenstein et al. (2022), the paleo-records do not always reflect the large-scale patterns. On the other hand, previous paleo-record studies have demonstrated that the $\delta^{18}\text{O}$ speleothems can capture the monsoon general pattern (Azevedo et al. 2021; Novello et al. 2018). Therefore, the SAMS numerical modeling in TraCE-21k reasonably detects the general variability patterns of the monsoon.

How does the spatial and temporal variability of the LISAM mode changes in each subperiod of the 21,000 years?

To answer this question, the EOF analysis was repeated for each individual subperiod (Figs. 4 and 5). The EOF1 and EOF2 spatial patterns were shown to have a strong relationship with freshwater pulses. In general, during the NH cold periods (H1 and YD), LISAM precipitation regime changes due to the southward ITCZ displacement, and, consequently, an increase in the NEB and CAM precipitation (Fig. 3), in agreement with the paleo-records. In addition, the mean tropospheric circulation in the monsoon region, with more intense northerly trade winds, causes changes in the Low-Level Jet from a N/S orientation to NW/SE direction (as shown in Fig. S5). Thus, the H1 and YD LISAM pattern is very similar to LISAM observed for the entire 21,000-year period. A similar pattern was observed for the EH, but with lower intensity due to the climatic transition which is characteristic of this subperiod.

BA is the only period that simultaneously features MWF in the Southern and Northern Hemispheres. Thus, the significant disturbance due to the NH heating, associated with the AMOC strength increase, shifting the ITCZ to the north. These significant changes modify the order in the EOF first two leading modes. Thus, the LISAM mode appears now represented by the EOF2, with 17.9% of the explained variance. Therefore, the EOF1 shows that 38.5% of the explained variance for the period is associated with latitudinal changes in the ITCZ position.

The MH, on the other hand, is also connected to the ITCZ northward shift due to the stronger AMOC intensity. Thus, the MH precipitation is characterized by an anomaly pattern concentrated in the CAM region with an extension to SEB, in addition to having an ITCZ close to 10°N , similar to the historical period position.

LH also shows an inversion in the order of the two leading variability modes, with 18.7% (16.8%) explained variance for EOF1 (EOF2). This period is the only one that does not have any MWF forcing in the simulation, which contributes to the fact that the leading modes are not clearly separated.

In all subperiods, the EOF1 and EOF2 patterns also show strong correlation with SASD, as found by Wainer et al.

(2021). During the cold (hot) periods, the SASD is negative (positive), favoring the precipitation displacement to the NEB (South/ SEB).

What is the role of each individual climatic forcing in driving SAMS?

By identifying the SAMS and SACZ spatial variability patterns during the 21 ka subperiods, we also aimed understanding the role of each individual climatic forcing in driving SAMS by applying LISAM for the 21,000 years for the single forcing and FULL experiments (Figs. 8 and 9). In general, the time series, normalized by their respective standard deviation of the EOF1 expansion coefficients, showed correlations between the single forcing experiments with the FULL experiment: GHG: 92.2%, ICE: 89.8%, MWF: 75.9%, ORB: 71.4%.

The EOF1 of the H1 and YD subperiods, is strongly coupled to the MWF experiment. In addition, YD is also related to the GHG and ORB variation. The observed changes in the NEB precipitation and southward migration of the ITCZ in the H1 and YD are connected to the insolation decrease in the NH, the freshwater pulses, and the reduction of greenhouse gases. For EOF2, orbital forcing is the leading forcing (60.5% correlation) in the precipitation modulation and ICE corresponds to -22.2% correlation.

Therefore, although the freshwater forcing does not have the largest correlation in the analysis of the entire 21 ka period, they are linked to the changes observed in the SAMS during H1, YD, and BA. The SACZ pattern, on the other hand, has a strong influence from changes in the orbital parameters, so that the SACZ southward migration observed throughout Holocene is mainly modulated by insolation, being verified in both modes (SAMS and oceanic SACZ).

How the multidecadal and millennial variability changes over the last 21 ka?

The multidecadal and millennial variability of the EOFs time series were investigated using wavelets (Figs. 8 and 9) for each subperiod and single forcing experiment.

In general, results indicate clear differences in the frequencies and spectral energy for the FULL and MWF experiments compared to the others, with very little power in the variability modes with period below 640 years. All experiments have most of the spectral energy at the lowest frequencies, i.e., with periods above 2560 years. The FULL and MWF experiments show a funnel-shaped energy transfer to higher frequencies at about 15 ka BP, consistent with the abrupt changes in the BA freshwater pulses and indicating that the series has a significant discontinuity due to this freshwater factor. Furthermore, the GHG and ICE experiments also illustrate the greenhouse gases and polar ice cover influence on SAMS during H1 and YD. Particularly,

the ICE experiment also shows an energy transfer to the higher frequencies (Period of the order of 2 ka) during the BA, representing the influence of the thaw due to the NH heating. The analysis also shows a significant periodicity in the FULL experiment (around 30 years period), consistent with a multidecadal variability mainly coupled with orbital and ice forcing.

As for the EOF2 case (SACZ), most experiments show energy confined in high-frequency modes (period below 640 years), with a peak at approximately 30–80 years, showing the importance of multidecadal patterns, such as the PDO and the AMO, in the precipitation of the oceanic SACZ (Chen et al. 2021).

The wavelet analysis for the FULL experiment considering each of the subperiods defined in Table 3, show that the multidecadal to centennial variability (period shorter than 320 years) have little spectral energy during H1 and BA. An increase in high-frequency variability begins to be noticed from the EH, which is intensified in the MH and LH.

Therefore, SAMS and the precipitation associated with the oceanic SACZ are strongly influenced by the meltwater discharge and, in specific periods, by the orbital and greenhouse gases forcing. In particular, the SACZ southward shift in the recent period has had a strong impact from orbital forcing and the insolation increase. Pacific and Atlantic multidecadal variability is identified in the TraCE-21k experiment only starting from the MH period, consistent with the previous studies (Chiessi et al. 2009; Zilli et al. 2019; Wainer et al. 2021; Chen et al. 2021). Thus, understanding how SAMS variability has changed in past climates is important to validate future scenarios and for studies on attribution of causes for observed climate changes (natural and anthropogenically driven).

Supplementary Information The online version contains supplementary material available at <https://doi.org/10.1007/s00382-024-07139-9>.

Acknowledgements The authors thank FAPESP for funding this study. The authors thank NOAA CPC and Earth System Research Laboratory Physical Sciences Laboratory for making available the data from the 20th Century Reanalysis, version 3, and from GPCP. They also thank NCAR for the availability of the TraCE-21k simulations.

Author contributions All authors have made substantial contributions to this submission and reviewed the article. ISC is responsible for performing the analysis and writing the paper. PLSD, IW, and LFP were essential in the orienting process, reviewing and discussing the paper. PD is the IC doctoral supervisor.

Funding Fundação de Amparo à Pesquisa do Estado de São Paulo (FAPESP) funded this study in the doctoral grant (2017/05285-4) and the PACMEDY/FAPESP project (2015/50686-1).

Data availability The TraCE-21k datasets is available at <https://www.earthsystemgrid.org/project/trace.html>. The R20C datasets can be downloaded from https://psl.noaa.gov/data/gridded/data.20thC_ReanV3.html. The GPCP precipitation data can be accessed at <https://psl.noaa.gov/data/gridded/data.gpcp.html>.

Declarations

Conflict of interest The authors declare that they have no known competing financial interests or personal relationships that could have appeared to influence the work reported in this paper.

Ethical approval and consent to participate Not applicable.

Consent for publication The authors gave their consent for the paper's publication.

References

- Addison PS (2018) Introduction to redundancy rules: the continuous wavelet transform comes of age. *Philos Trans R Soc A Math Phys Eng Sci* 376:20170258. <https://doi.org/10.1098/rsta.2017.0258>
- Adler R, Wang JJ, Sapiano M et al (2016) Global precipitation climatology project (GPCP) climate data record (CDR), Version 2.3 (Monthly). National Centers for Environmental Information 10:V56971M6
- Aguiar W, Prado LF, Wainer I et al (2020) Freshwater forcing control on early-Holocene South American monsoon. *Quat Sci Rev* 245:106498. <https://doi.org/10.1016/j.quascirev.2020.106498>
- Apaéstegui J, Cruz FW, Sifeddine A et al (2014) Hydroclimate variability of the northwestern Amazon Basin near the Andean foothills of Peru related to the South American Monsoon System during the last 1600 years. *Clim past* 10:1967–1981. <https://doi.org/10.5194/cp-10-1967-2014>
- Azevedo V, Strikis NM, Novello VF et al (2021) Paleovegetation seesaw in Brazil since the Late Pleistocene: a multiproxy study of two biomes. *Earth Planet Sci Lett* 563:116880. <https://doi.org/10.1016/j.epsl.2021.116880>
- Barros V, Gonzalez M, Liebmann B, Camilloni I (2000) Influence of the South Atlantic convergence zone and South Atlantic Sea surface temperature on interannual summer rainfall variability in Southeastern South America. *Theor Appl Climatol* 67:123–133. <https://doi.org/10.1007/s007040070002>
- Berger AL (1978) Long-term variations of daily insolation and quaternary climatic changes. *J Atmos Sci* 35:2361–2367. [https://doi.org/10.1175/1520-0469\(1978\)035%3c2362:ltvodi%3e2.0.co;2](https://doi.org/10.1175/1520-0469(1978)035%3c2362:ltvodi%3e2.0.co;2)
- Bernal JP, Cruz FW, Strikis NM et al (2016) High-resolution Holocene South American monsoon history recorded by a speleothem from Botuverá Cave, Brazil. *Earth Planet Sci Lett* 450:186–196. <https://doi.org/10.1016/j.epsl.2016.06.008>
- Bombardi RJ, Carvalho LMV, Jones C, Reboita MS (2014) Precipitation over eastern South America and the South Atlantic Sea surface temperature during neutral ENSO periods. *Clim Dyn* 42:1553–1568. <https://doi.org/10.1007/s00382-013-1832-7>
- Braconnot P, Harrison SP, Kageyama M et al (2012) Evaluation of climate models using palaeoclimatic data. *Nat Clim Chang* 2:417–424. <https://doi.org/10.1038/nclimate1456>
- Carvalho LMV, Cavalcanti IFA (2016) The South American Monsoon System (SAMS). In: de Carvalho LMV, Jones C (eds) *The monsoons and climate change: observations and modeling*. Springer, Cham, pp 121–148
- Carvalho LMV, Jones C, Liebmann B (2002) Extreme precipitation events in southeastern south America and large-scale convective patterns in the south Atlantic convergence zone. *J Clim* 15:2377–2394. [https://doi.org/10.1175/1520-0442\(2002\)015%3c2377:EPEISS%3e2.0.CO;2](https://doi.org/10.1175/1520-0442(2002)015%3c2377:EPEISS%3e2.0.CO;2)
- Carvalho LMV, Jones C, Liebmann B (2004) The South Atlantic Convergence Zone: intensity, form, persistence, and relationships with intraseasonal to interannual activity and extreme rainfall. *J*

- Clim 17:88–108. [https://doi.org/10.1175/1520-0442\(2004\)017%3c0088:TSACZI%3e2.0.CO;2](https://doi.org/10.1175/1520-0442(2004)017%3c0088:TSACZI%3e2.0.CO;2)
- Carvalho LMV, Jones C, Silva AE et al (2011) The South American Monsoon System and the 1970s climate transition. *Int J Climatol* 31:1248–1256. <https://doi.org/10.1002/joc.2147>
- Carvalho LMV, Jones C, Cannon F, Norris J (2016) Intraseasonal-to-interannual variability of the Indian monsoon identified with the large-scale index for the Indian Monsoon System (LIMS). *J Clim* 29:2941–2962. <https://doi.org/10.1175/JCLI-D-15-0423.1>
- Casarin DP, Kousky VE (1986) Anomalias de precipitação no sul do Brasil e variações na circulação atmosférica. *Rev Brasil Meteorol* 1:83–90
- Chaves RR (2004) Interactions between sea surface temperature over the South Atlantic Ocean and the South Atlantic Convergence Zone. *Geophys Res Lett* 31:L03204. <https://doi.org/10.1029/2003GL018647>
- Chen C, Zhao W, Zhang X (2021) Pacific Decadal Oscillation-like variability at a millennial timescale during the Holocene. *Glob Planet Change* 199:103448. <https://doi.org/10.1016/j.gloplacha.2021.103448>
- Chiang JCH, Vimont DJ (2004) Analogous Pacific and Atlantic meridional modes of tropical atmosphere–ocean variability. *J Clim* 17:4143–4158. <https://doi.org/10.1175/JCLI4953.1>
- Chiessi CM, Mulitza S, Pätzold J et al (2009) Possible impact of the Atlantic Multidecadal Oscillation on the South American summer monsoon. *Geophys Res Lett* 36:L21707. <https://doi.org/10.1029/2009GL039914>
- Compo GP, Whitaker JS, Sardeshmukh PD et al (2011) The twentieth century reanalysis project. *Q J R Meteorol Soc* 137:1–28. <https://doi.org/10.1002/qj.776>
- Cruz FW, Burns SJ, Karmann I et al (2005) Insolation-driven changes in atmospheric circulation over the past 116,000 years in subtropical Brazil. *Nature* 434:63–66. <https://doi.org/10.1038/nature03365>
- Cruz FW, Burns SJ, Jercinovic M et al (2007) Evidence of rainfall variations in Southern Brazil from trace element ratios (Mg/Ca and Sr/Ca) in a Late Pleistocene stalagmite. *Geochim Cosmochim Acta* 71:2250–2263. <https://doi.org/10.1016/j.gca.2007.02.005>
- Cruz FW, Vuille M, Burns SJ et al (2009) Orbitally driven east–west antiphasing of South American precipitation. *Nat Geosci* 2:210–214. <https://doi.org/10.1038/ngeo444>
- da Silva AE, de Carvalho LMV (2007) Large-scale index for South America Monsoon (LISAM). *Atmos Sci Lett* 8:51–57. <https://doi.org/10.1002/asl.150>
- Deplazes G, Lückge A, Peterson LC et al (2013) Links between tropical rainfall and North Atlantic climate during the last glacial period. *Nat Geosci* 6:213–217. <https://doi.org/10.1038/ngeo1712>
- Donohoe A, Marshall J, Ferreira D, McGee D (2013) The relationship between ITCZ location and cross-equatorial atmospheric heat transport: from the seasonal cycle to the last glacial maximum. *J Clim* 26:3597–3618. <https://doi.org/10.1175/JCLI-D-12-00467.1>
- Gan MA, Kousky VE, Ropelewski CF (2004) The South America Monsoon circulation and its relationship to rainfall over West-Central Brazil. *J Clim* 17:47–66. [https://doi.org/10.1175/1520-0442\(2004\)017%3c0047:TSAMCA%3e2.0.CO;2](https://doi.org/10.1175/1520-0442(2004)017%3c0047:TSAMCA%3e2.0.CO;2)
- Gandu AW, Silva Dias PL (1998) Impact of tropical heat sources on the South American tropospheric upper circulation and subsidence. *J Geophys Res Atmos* 103:6001–6015. <https://doi.org/10.1029/97JD03114>
- Garcia SR, Kayano MT (2009) Determination of the onset dates of the rainy season in central Amazon with equatorially antisymmetric outgoing longwave radiation. *Theor Appl Climatol* 97:361–372. <https://doi.org/10.1007/s00704-008-0080-y>
- Garcia SR, Kayano MT (2013) Some considerations on onset dates of the rainy season in Western-Central Brazil with antisymmetric outgoing longwave radiation relative to the equator. *Int J Climatol* 33:188–198. <https://doi.org/10.1002/joc.3417>
- Garcia SR, Kayano MT (2015) Multidecadal variability of moisture and heat budgets of the South American monsoon system. *Theor Appl Climatol* 121:557–570. <https://doi.org/10.1007/s00704-014-1265-1>
- Garcia SR, Kayano MT, Calheiros AJP et al (2017) Moisture and heat budgets of the south American monsoon system: climatological aspects. *Theor Appl Climatol* 130:233–247. <https://doi.org/10.1007/s00704-016-1882-y>
- Gorenstein I, Prado LF, Bianchini PR et al (2022) A fully calibrated and updated mid-Holocene climate reconstruction for Eastern South America. *Quat Sci Rev* 292:107646. <https://doi.org/10.1016/j.quascirev.2022.107646>
- He F (2011) Simulating transient climate evolution of the last deglaciation with CCSM 3. PhD Thesis, University of Wisconsin
- He P, Liu J, Wang B, Sun W (2021) Understanding global monsoon precipitation changes during the 8.2 ka event and the current warm period. *Palaeogeogr Palaeoclimatol Palaeoecol*. <https://doi.org/10.1016/j.palaeo.2021.110757>
- Hughen KA, Overpeck JT, Peterson LC, Trumbore S (1996) Rapid climate changes in the tropical Atlantic region during the last deglaciation. *Nature* 380:51–54. <https://doi.org/10.1038/380051a0>
- Jones C, Carvalho LMV (2002) Active and break phases in the South American Monsoon System. *J Clim* 15:905–914. [https://doi.org/10.1175/1520-0442\(2002\)015%3c0905:AABPIT%3e2.0.CO;2](https://doi.org/10.1175/1520-0442(2002)015%3c0905:AABPIT%3e2.0.CO;2)
- Joos F, Spahni R (2008) Rates of change in natural and anthropogenic radiative forcing over the past 20,000 years. *Proc Natl Acad Sci* 105(5):1425–1430. <https://doi.org/10.1073/pnas.0707386105>
- Jorgetti T, da Silva Dias PL, de Freitas ED (2014) The relationship between South Atlantic SST and SACZ intensity and positioning. *Clim Dyn* 42:3077–3086. <https://doi.org/10.1007/s00382-013-1998-z>
- Kodama Y (1992) Large-scale common features of subtropical precipitation zones (the Baiu Frontal Zone, the SPCZ, and the SACZ) Part I: characteristics of subtropical frontal zones. *J Meteorol Soc Jpn Ser II* 70:813–836. https://doi.org/10.2151/jmsj1965.70.4_813
- Kodama Y-M (1993) Large-scale common features of sub-tropical convergence zones (the Baiu Frontal Zone, the SPCZ, and the SACZ) Part II: conditions of the circulations for generating the STCZs. *J Meteorol Soc Jpn Ser II* 71:581–610. https://doi.org/10.2151/jmsj1965.71.5_581
- Kousky VE (1988) Pentad outgoing longwave radiation climatology for the South American sector. *Rev Brasil Meteorol* 3:217–231
- Kutzbach J, Gallimore R, Harrison S et al (1998) Climate and biome simulations for the past 21,000 years. *Quat Sci Rev* 17:473–506. [https://doi.org/10.1016/S0277-3791\(98\)00009-2](https://doi.org/10.1016/S0277-3791(98)00009-2)
- Liebmann B, Mechoso CR (2011) The South American Monsoon System. In: *The global monsoon system: research and forecast*, pp 137–157. https://doi.org/10.1142/9789814343411_0009
- Liebmann B, Jones C, de Carvalho LMV (2001) Interannual variability of daily extreme precipitation events in the state of São Paulo, Brazil. *J Clim* 14:208–218. [https://doi.org/10.1175/1520-0442\(2001\)014%3c0208:IVODEP%3e2.0.CO;2](https://doi.org/10.1175/1520-0442(2001)014%3c0208:IVODEP%3e2.0.CO;2)
- Liu Z, Otto-Bliessner BL, He F et al (2009) Transient simulation of last deglaciation with a new mechanism for Bølling-Allerød warming. *Science* (1979) 325:310–314. <https://doi.org/10.1126/science.1171041>
- Liu Z, Carlson AE, He F et al (2012) Younger Dryas cooling and the Greenland climate response to CO₂. *Proc Natl Acad Sci* 109:11101–11104. <https://doi.org/10.1073/pnas.1202183109>
- Liu W, Liu Z, Cheng J, Hu H (2015) On the stability of the Atlantic meridional overturning circulation during the last deglaciation. *Clim Dyn* 44:1257–1275. <https://doi.org/10.1007/s00382-014-2153-1>

- Liu X, Battisti DS, Donohoe A (2017) Tropical precipitation and cross-equatorial ocean heat transport during the mid-Holocene. *J Clim* 30(10):3529–3547
- Lutsko NJ, Marshall J, Green B (2019) Modulation of monsoon circulations by cross-equatorial ocean heat transport. *J Clim* 32:3471–3485. <https://doi.org/10.1175/JCLI-D-18-0623.1>
- Mantua NJ, Hare SR (2002) The Pacific Decadal oscillation. *J Oceanogr* 58:35–44. <https://doi.org/10.1023/A:1015820616384>
- Marengo JA, Liebmann B, Grimm AM et al (2012) Recent developments on the South American monsoon system. *Int J Climatol* 32:1–21. <https://doi.org/10.1002/joc.2254>
- Marshall J, Donohoe A, Ferreira D, McGee D (2014) The ocean's role in setting the mean position of the Inter-Tropical Convergence Zone. *Clim Dyn* 42:1967–1979. <https://doi.org/10.1007/s00382-013-1767-z>
- Marson JM, Wainer I, Mata MM, Liu Z (2014) The impacts of deglacial meltwater forcing on the South Atlantic Ocean deep circulation since the Last Glacial Maximum. *Clim past* 10:1723–1734. <https://doi.org/10.5194/cp-10-1723-2014>
- McGee D, Donohoe A, Marshall J, Ferreira D (2014) Changes in ITCZ location and cross-equatorial heat transport at the Last Glacial Maximum, Heinrich Stadial 1, and the mid-Holocene. *Earth Planet Sci Lett* 390:69–79. <https://doi.org/10.1016/j.epsl.2013.12.043>
- McGee D, Moreno-Chamarro E, Green B et al (2018) Hemispherically asymmetric trade wind changes as signatures of past ITCZ shifts. *Quat Sci Rev* 180:214–228. <https://doi.org/10.1016/j.quascirev.2017.11.020>
- Mohtadi M, Prange M, Steinke S (2016) Palaeoclimatic insights into forcing and response of monsoon rainfall. *Nature* 533:191–199. <https://doi.org/10.1038/nature17450>
- Moreno-Chamarro E, Marshall J, Delworth TL (2020) Linking ITCZ migrations to the AMOC and North Atlantic/Pacific SST decadal variability. *J Clim* 33:893–905. <https://doi.org/10.1175/JCLI-D-19-0258.1>
- Mulitza S, Chiessi CM, Schefuß E et al (2017) Synchronous and proportional deglacial changes in Atlantic meridional overturning and northeast Brazilian precipitation. *Paleoceanography* 32:622–633. <https://doi.org/10.1002/2017PA003084>
- Nogués-Paegle J, Mo KC (1997) Alternating wet and dry conditions over South America during summer. *Mon Weather Rev* 125:279–291
- Novello VF, Cruz FW, Karmann I et al (2012) Multidecadal climate variability in Brazil's Nordeste during the last 3000 years based on speleothem isotope records. *Geophys Res Lett*. <https://doi.org/10.1029/2012GL053936>
- Novello VF, Cruz FW, Vuille M et al (2017) A high-resolution history of the South American Monsoon from Last Glacial Maximum to the Holocene. *Sci Rep* 7:44267. <https://doi.org/10.1038/srep44267>
- Novello VF, Cruz, FW, Moquet JS, Vuille M, de Paula MS, Nunes D et al (2018) Two millennia of South Atlantic Convergence Zone variability reconstructed from isotopic proxies. *Geophys Res Lett* 45:5045–5051. <https://doi.org/10.1029/2017GL076838>
- Novello VF, Cruz FW, McGlue MM et al (2019) Vegetation and environmental changes in tropical South America from the last glacial to the Holocene documented by multiple cave sediment proxies. *Earth Planet Sci Lett* 524:115717. <https://doi.org/10.1016/j.epsl.2019.115717>
- Novello VF, William da Cruz F, Vuille M et al (2021) Investigating $\delta^{13}C$ values in stalagmites from tropical South America for the last two millennia. *Quat Sci Rev* 255:106822. <https://doi.org/10.1016/j.quascirev.2021.106822>
- Obase T, Abe-Ouchi A (2019) Abrupt Bølling-Allerød warming simulated under gradual forcing of the last deglaciation. *Geophys Res Lett* 46:11397–11405. <https://doi.org/10.1029/2019GL084675>
- Orrison R, Vuille M, Smerdon JE, Apaéstegui J, Azevedo V, Campos JLP, Cruz FW, Della Libera ME, Stríkis NM (2022) South American Summer Monsoon variability over the last millennium in paleoclimate records and isotope-enabled climate models. *Clim past* 18(9):2045–2062
- Otto-Bliiesner BL, Marshall SJ, Overpeck JT et al (2006) Simulating arctic climate warmth and icefield retreat in the last interglaciation. *Science* (1979) 311:1751–1753. <https://doi.org/10.1126/science.1120808>
- Rao VB, Cavalcanti IFA, Hada K (1996) Annual variation of rainfall over Brazil and water vapor characteristics over South America. *J Geophys Res Atmos* 101:26539–26551. <https://doi.org/10.1029/96JD01936>
- Robertson AW, Mechoso CR (2000) Interannual and interdecadal variability of the South Atlantic Convergence Zone. *Mon Weather Rev* 128(8):2947–2957. [https://doi.org/10.1175/1520-0493\(2000\)128%3C2947:IAIVOT%3E2.0.CO;2](https://doi.org/10.1175/1520-0493(2000)128%3C2947:IAIVOT%3E2.0.CO;2)
- Santos TP, Shimizu MH, Nascimento RA et al (2022) A data-model perspective on the Brazilian margin surface warming from the Last Glacial Maximum to the Holocene. *Quat Sci Rev* 286:107557. <https://doi.org/10.1016/j.quascirev.2022.107557>
- Schneider T (2017) Feedback of atmosphere-ocean coupling on shifts of the intertropical convergence zone. *Geophys Res Lett* 44:11644–11653. <https://doi.org/10.1002/2017GL075817>
- Stríkis NM, Cruz FW, Cheng H et al (2011) Abrupt variations in South American monsoon rainfall during the Holocene based on a speleothem record from central-eastern Brazil. *Geology* 39:1075–1078. <https://doi.org/10.1130/G32098.1>
- Stríkis NM, Chiessi CM, Cruz FW et al (2015) Timing and structure of Mega-SACZ events during Heinrich Stadial 1. *Geophys Res Lett* 42:5477–5484A. <https://doi.org/10.1002/2015GL064048>
- Stríkis NM, Cruz FW, Barreto EAS et al (2018) South American monsoon response to iceberg discharge in the North Atlantic. *Proc Natl Acad Sci* 115:3788–3793. <https://doi.org/10.1073/pnas.1717784115>
- Talento S, Barreiro M (2012) Estimation of natural variability and detection of anthropogenic signal in summertime precipitation over South America. *Adv Meteorol* 2012:1–10. <https://doi.org/10.1155/2012/725343>
- Talento S, Barreiro M (2018) Control of the South Atlantic Convergence Zone by extratropical thermal forcing. *Clim Dyn* 50:885–900. <https://doi.org/10.1007/s00382-017-3647-4>
- Utida G, Cruz FW, Santos RV et al (2020) Climate changes in North-eastern Brazil from deglacial to Meghalayan periods and related environmental impacts. *Quat Sci Rev* 250:106655. <https://doi.org/10.1016/j.quascirev.2020.106655>
- Venancio IM, Shimizu MH, Santos TP et al (2020) Changes in surface hydrography at the western tropical Atlantic during the Younger Dryas. *Glob Planet Change* 184:103047. <https://doi.org/10.1016/j.gloplacha.2019.103047>
- Vera C, Higgins W, Amador J et al (2006) Toward a unified view of the American Monsoon Systems. *J Clim* 19:4977–5000. <https://doi.org/10.1175/JCLI3896.1>
- Vera CS, Alvarez MS, Gonzalez PLM et al (2018) Seasonal cycle of precipitation variability in South America on intraseasonal timescales. *Clim Dyn* 51:1991–2001. <https://doi.org/10.1007/s00382-017-3994-1>
- Vuille M, Burns SJ, Taylor BL et al (2012) A review of the South American monsoon history as recorded in stable isotopic proxies over the past two millennia. *Clim past* 8:1309–1321. <https://doi.org/10.5194/cp-8-1309-2012>
- Wainer I, Venegas SA (2002) South Atlantic multidecadal variability in the climate system model. *J Clim* 15:1408–1420. [https://doi.org/10.1175/1520-0442\(2002\)015%3c1408:SAMVIT%3e2.0.CO;2](https://doi.org/10.1175/1520-0442(2002)015%3c1408:SAMVIT%3e2.0.CO;2)
- Wainer I, Prado LF, Khodri M, Otto-Bliiesner B (2015) Reconstruction of the South Atlantic Subtropical Dipole index for the past 12,000

- years from surface temperature proxy. *Sci Rep* 4:5291. <https://doi.org/10.1038/srep05291>
- Wainer I, Prado LF, Khodri M, Otto-Bliesner B (2021) The South Atlantic sub-tropical dipole mode since the last deglaciation and changes in rainfall. *Clim Dyn* 56:109–122. <https://doi.org/10.1007/s00382-020-05468-z>
- Walker M, Gibbard P, Head MJ et al (2019) Formal Subdivision of the Holocene Series/Epoch: a Summary. *J Geol Soc India* 93:135–141. <https://doi.org/10.1007/s12594-019-1141-9>
- Wang X, Edwards RL, Auler AS et al (2017) Hydroclimate changes across the Amazon lowlands over the past 45,000 years. *Nature* 541:204–207. <https://doi.org/10.1038/nature20787>
- Ward BM, Wong CI, Novello VF et al (2019) Reconstruction of Holocene coupling between the South American Monsoon System and local moisture variability from speleothem $\delta^{18}\text{O}$ and $^{87}\text{Sr}/^{86}\text{Sr}$ records. *Quat Sci Rev* 210:51–63. <https://doi.org/10.1016/j.quascirev.2019.02.019>
- Wen X, Liu Z, Wang S et al (2016) Correlation and anti-correlation of the East Asian summer and winter monsoons during the last 21,000 years. *Nat Commun* 7:11999. <https://doi.org/10.1038/ncomms11999>
- Wortham BE, Wong CI, Silva LCR et al (2017) Assessing response of local moisture conditions in central Brazil to variability in regional monsoon intensity using speleothem $^{87}\text{Sr}/^{86}\text{Sr}$ values. *Earth Planet Sci Lett* 463:310–322. <https://doi.org/10.1016/j.epsl.2017.01.034>
- Zhou J, Lau K-M (1998) Does a monsoon climate exist over South America? *J Clim* 11:1020–1040. [https://doi.org/10.1175/1520-0442\(1998\)011%3c1020:DAMCEO%3e2.0.CO;2](https://doi.org/10.1175/1520-0442(1998)011%3c1020:DAMCEO%3e2.0.CO;2)
- Zilli MT, Carvalho LMV, Lintner BR (2019) The poleward shift of South Atlantic Convergence Zone in recent decades. *Clim Dyn* 52:2545–2563. <https://doi.org/10.1007/s00382-018-4277-1>

Publisher's Note Springer Nature remains neutral with regard to jurisdictional claims in published maps and institutional affiliations.

Springer Nature or its licensor (e.g. a society or other partner) holds exclusive rights to this article under a publishing agreement with the author(s) or other rightsholder(s); author self-archiving of the accepted manuscript version of this article is solely governed by the terms of such publishing agreement and applicable law.